

NAVAL POSTGRADUATE SCHOOL

Monterey, California



THESIS

**RADAR OBSERVATIONS OF FIELD-ALIGNED
PLASMA PROPAGATIONS ASSOCIATED WITH
NASA'S PMG EXPERIMENT**

by

Darren Montgomery Olson

September 1994

Thesis Advisor:

R.C. Olsen

Approved for public release; distribution is unlimited.

REPORT DOCUMENTATION PAGE			Form Approved OMB No. 0704	
Public reporting burden for this collection of information is estimated to average 1 hour per response, including the time for reviewing instruction, searching existing data sources, gathering and maintaining the data needed, and completing and reviewing the collection of information. Send comments regarding this burden estimate or any other aspect of this collection of information, including suggestions for reducing this burden, to Washington Headquarters Services				
1. AGENCY USE ONLY (Leave blank)		2. REPORT DATE September 1994	3. REPORT TYPE AND DATES COVERED Master's Thesis	
4. TITLE AND SUBTITLE RADAR OBSERVATIONS OF FIELD-ALIGNED PLASMA PROPAGATIONS ASSOCIATED WITH NASA'S PMG EXPERIMENT			5. FUNDING NUMBERS	
6. AUTHOR(S) Darren Montgomery Olson				
7. PERFORMING ORGANIZATION NAME(S) AND ADDRESS(ES) Naval Postgraduate School Monterey CA 93943-5000			8. PERFORMING ORGANIZATION REPORT NUMBER	
9. SPONSORING/MONITORING AGENCY NAME(S) AND ADDRESS(ES)			10. SPONSORING/MONITORING AGENCY REPORT NUMBER	
11. SUPPLEMENTARY NOTES The views expressed in this thesis are those of the author and do not reflect the official policy or position of the Department of Defense or the U.S. Government.				
12a. DISTRIBUTION/AVAILABILITY STATEMENT Approved for public release; distribution is unlimited.			12b. DISTRIBUTION CODE *A	
13. ABSTRACT (maximum 200 words) NASA's Plasma Motor Generator (PMG) tethered satellite mission was launched in June 1993 to verify the ability of hollow cathode plasma sources to couple electric currents from an electrodynamic tether into the ambient ionospheric plasma. This large-scale coupling process resulted in turbulent plasma signatures associated with the orbiting plasma generator, which propagated over great distances along the earth's geomagnetic field lines. VHF radars in Hilo, Hawaii and Jicamarca, Peru recorded observations of these field-aligned disturbances as part of the experiment. Based on analysis of these radar observations and tracking data of PMG's orbit, the effective propagation velocity of these traveling plasma waveforms was calculated to be of the order of 1000 meters per second. Detection of these disturbances, associated with PMG's passage overhead, supports the existence of a phantom current loop allowing current flow along the magnetic field lines of the earth and into the lower ionosphere from either end of an electrodynamic tether.				
14. SUBJECT TERMS Electrodynamic Tether, Hollow Cathode Plasma Source, Plasma Motor/Generator, NASA Experiment			15. NUMBER OF PAGES 97	
			16. PRICE CODE	
17. SECURITY CLASSIFICATION OF REPORT Unclassified	18. SECURITY CLASSIFICATION OF THIS PAGE Unclassified	19. SECURITY CLASSIFICATION OF ABSTRACT Unclassified	20. LIMITATION OF ABSTRACT UL	

NSN 7540-01-280-5500

Standard Form 298 (Rev. 2-89)
Prescribed by ANSI Std. Z39-18

Approved for public release; distribution is unlimited.

Radar Observations of Field-Aligned Plasma Propagations
Associated with NASA's PMG Experiment

by

Darren M. Olson
Lieutenant, United States Navy
B.S.E., United States Naval Academy, 1988

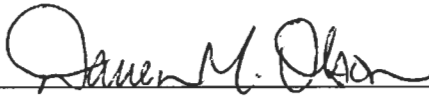
Submitted in partial fulfillment
of the requirements for the degree of

MASTER OF SCIENCE IN SYSTEMS TECHNOLOGY
(SPACE SYSTEMS OPERATIONS)

from the

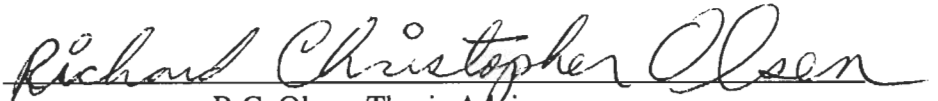
NAVAL POSTGRADUATE SCHOOL
September 1994

Author:

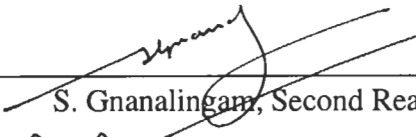


Darren M. Olson

Approved by:



R.C. Olsen, Thesis Advisor



S. Gnanalingam, Second Reader



R. Panholzer, Chairman
Space Systems Academic Group

ABSTRACT

NASA's Plasma Motor Generator (PMG) tethered satellite mission was launched in June 1993 to verify the ability of hollow cathode plasma sources to couple electric currents from an electrodynamic tether into the ambient ionospheric plasma. This large-scale coupling process resulted in turbulent plasma signatures associated with the orbiting plasma generator, which propagated over great distances along the earth's geomagnetic field lines. VHF radars in Hilo, Hawaii and Jicamarca, Peru recorded observations of these field-aligned disturbances as part of the experiment. Based on analysis of these radar observations and tracking data of PMG's orbit, the effective propagation velocity of these traveling plasma waveforms was calculated to be of the order of 1000 meters per second. Detection of these disturbances, associated with PMG's passage overhead, supports the existence of a phantom current loop allowing current flow along the magnetic field lines of the earth and into the lower ionosphere from either end of an electrodynamic tether.

TABLE OF CONTENTS

I.	INTRODUCTION.....	1
II.	BACKGROUND ON TETHERS.....	5
	A. HISTORY.....	5
	B. GRAVITY-GRADIENT STABILIZATION.....	7
	C. ELECTRODYNAMIC TETHERS.....	10
III.	THE SPACE ENVIRONMENT.....	17
	A. EARTH'S GEOMAGNETIC FIELD.....	17
	B. IONOSPHERIC PLASMA.....	19
IV.	THE PMG EXPERIMENT.....	21
	A. MISSION OBJECTIVES.....	21
	B. PHYSICAL DESCRIPTION.....	22
	C. FLIGHT PROFILE.....	24
	D. RADAR OBSERVATION SITES.....	24
V.	EXPERIMENTAL OBSERVATIONS AND ANALYSIS.....	29
	A. HAWAII PASSES.....	29
	B. JICAMARCA PASSES.....	34
	1. PASS 2.....	35
	2. PASS 3.....	37
	3. PASS 4.....	38
VI.	SUMMARY AND DISCUSSION.....	41
VII.	CONCLUSIONS.....	47
	LIST OF REFERENCES.....	79
	INITIAL DISTRIBUTION LIST.....	81

LIST OF FIGURES AND TABLES

FIGURE 1: Early Gravity-Gradient Concepts.....	49
FIGURE 2: Forces Acting on Tethered Satellites.....	50
FIGURE 3: Restoring Forces Acting on Tethered Satellites.....	51
FIGURE 4: Current Paths for Electrodynamic Tethers.....	52
FIGURE 5: The Phantom Current Loop.....	53
FIGURE 6: The Generator Principle.....	54
FIGURE 7: The Motor Principle.....	55
FIGURE 8: The Eccentric-Dipole Model of the Earth's Magnetic Field.....	56
FIGURE 9: Geometry for a Static Dipolar Field.....	57
FIGURE 10: Geometric Latitude and Equatorial Crossing of a Field Line.....	58
FIGURE 11: Ionospheric Electron Density Layers.....	59
FIGURE 12: PMG Hollow Cathode Assembly Schematic.....	60
FIGURE 13: PMG Mission Flight Profile.....	61
FIGURE 14: PMG Ground track and Observing Radar Sites.....	62
FIGURE 15: Hawaii Radar Beam Geometry for Pass 1.....	63
FIGURE 16: PMG Hawaii Pass 1 Echo Activity.....	64
FIGURE 17: Hawaii Pass 1 Plasma Returns - Range Gate 3.....	65
FIGURE 18: Hawaii Pass 1 Plasma Returns - Range Gates 4 and 5.....	66
FIGURE 19: Hawaii Pass 1 Plasma Returns - Range Gates 6 and 7.....	67
FIGURE 20: Geometry for Hawaii Pass 1 Calculations.....	68
FIGURE 21: Geometry for Jicamarca Pass 2 Calculations.....	69
FIGURE 22: Flux-Tube Height Variation Relative to Jicamarca.....	70

FIGURE 23: Geometry for Jicamarca Pass 3 and 4 Calculations..... 71

FIGURE 24: Formation of Alfven Wings..... 72

FIGURE 25: Formation of Whistler Wings..... 73

FIGURE 24: Whistler Mode Phase Velocity/Frequency Relationship..... 74

TABLE 1: PMG Meridian Crossing for Hawaii Pass 1..... 75

TABLE 2: PMG Meridian Crossing for Jicamarca Pass 2..... 76

TABLE 3: PMG Meridian Crossing for Jicamarca Pass 3..... 77

TABLE 4: PMG Meridian Crossing for Jicamarca Pass 4..... 78

ACKNOWLEDGMENTS

I would like to acknowledge my thesis advisor, Dr. Olsen, for his superb support and guidance. His expertise in the fields of plasma physics and the space environment has proven invaluable to me throughout the writing of this thesis, and resulted in this research being conducted in a most satisfying environment. I am deeply indebted to Dr. Jerry Jost and Greg McCaskill for their help, which ranged from providing experimental data and technical support to holding theoretical discussions, both of whom were always willing to answer my numerous questions. Dr. Jim McCoy's involvement in orchestrating the successful PMG experiment is also deserving of special note.

In addition, I would like to thank my family - my parents, for their reassurance and constant encouragement, and my children who remain the pride and joy of my life. Most importantly, I thank my wife, for her never-ending understanding and patience during these last two years, whose love helped to make this thesis a reality. Her involvement in bringing this work to its final form is impossible to describe on these typewritten pages. The fruits of her labor are most appreciated.

I. INTRODUCTION

At approximately 13:27 GMT on June 26, 1993, an Air Force Delta-II rocket roared off the launch pad at Cape Canaveral, its third stage carrying a Global Positioning Satellite (GPS) as the primary payload. Attached to the second stage of the Delta-II was NASA's Plasma Motor Generator (PMG) tethered satellite mission. Following third stage separation and second stage fuel depletion burn, the PMG system was left in an elliptical orbit, approximately 207 x 922 kilometers, at a 27.5 degree inclination. At approximately 2000 seconds mission elapsed time, a Far End Package (FEP) was spring-ejected from the Delta-II second stage, at a rate of two to three meters per second, trailing a 500-meter conducting wire from the PMG tether deployer assembly. Within minutes, the two-body tethered satellite system stabilized in a gravity-gradient configuration with the FEP above the Delta-II second stage.

The primary objective of the PMG experiment was to verify the ability of hollow cathode plasma sources to couple electric currents from either end of a long wire moving through the ambient Low Earth Orbit (LEO) ionospheric plasma. By providing a low-impedance electrical connection with the ambient environment, while moving at orbital velocity through the earth's magnetic field, significant currents can be induced in a single-conductor tether wire, providing the capability for direct conversion of orbital energy to extractable electrical current (generator principle). Alternatively, orbital "steering" forces can be induced through the tether by driving current in the opposite direction with applied voltage (motor principle). The PMG experiment utilized these physical principles to investigate the overall practicality of reciprocal conversion of orbital energy and electricity, and also, to evaluate current technology for transferring charge

charge between a spacecraft and the LEO environment, utilizing hollow cathode plasma contactors.

The PMG electrodynamic tether orbited within the tenuous, electrically charged layer of the atmosphere known as the ionosphere, providing the opportunity to increase understanding of physical processes in the near-Earth space environment, while at the same time exploring the mechanical dynamics of tethered systems. A key mission objective was to investigate large-scale coupling processes and turbulent signatures associated with an orbiting artificial plasma generator and the ambient ionospheric plasma. The approach to accomplish this study utilized sensitive VHF meter-wave ionospheric radars to sense field-linked plasma perturbations at large distances from the orbiting plasma source. Near Lima, Peru, the powerful fifty megahertz radar at Jicamarca Radio Observatory was aligned to observe field-aligned backscatter from the near horizontal magnetic field lines. Two less sensitive fifty megahertz wind-profilers, located at Piura, Peru and Pohnpei, Micronesia, were configured for ionospheric measurements along the geomagnetic field lines. Additionally, NASA/JSC deployed a transportable radar system to Hilo, Hawaii, developed for remote field study of ionospheric modification effects, spacecraft interactions with the lower ionospheric environment, and reentering orbital debris.

Electromagnetic scattering from strong ionospheric turbulence generated during operation of the PMG experiment was observed from several of the VHF radar sites by radar probing of the geomagnetic flux tubes that mapped from the orbiter through the radar's fixed field-of-view. On several passes, field-aligned backscatter was observed from plasma structure propagating along the lines at distances up to several hundred kilometers from the PMG plasma source. The purpose of this thesis is to present these

observations, and develop the implications for the generation of field-aligned disturbances by the tether.

II. BACKGROUND ON TETHERS

"Come, let us build ourselves a city, with a tower that reaches to the heavens..."

-- The Tower of Babel, from the Book of Genesis, Chapter 11

A. HISTORY

The earliest concepts for the application of tethers in space can be traced back to the last century. In 1895 Kostantin Tsiolkovsky, the Russian schoolteacher and pioneer of astronautics, reflected on a way to create an environment devoid of terrestrial gravity through the construction of an equatorial tower pointing into space, reaching beyond geostationary altitude. He postulated that upon ascending such a "Heavenly Tower," the effects of gravity would gradually diminish until they disappeared completely. Although he did not realize it, Tsiolkovsky had conceived the first geostationary satellite.(Tsiolkovsky, 1895)

Sixty-five years later, at the dawn of the space age, the Leningrad engineer Yu Artsutanov conceived an alternate concept, consisting of a platform anchored in space, pointing towards the earth, with a cable deployed down from the satellite to connect it to the earth's surface at the equator. A second cable deployed upward beyond the satellite would carry a ballast to maintain the system's center of gravity in the geostationary orbit. Artsutanov visualized his "Heavenly Funicular" as a means of supporting transportation into space, and thus was born the idea of a space elevator.(Artsutanov, 1960)

The early 1960's saw a flurry of tether-related proposals, including concepts such as rolling satellites, lunar and asteroid tethers, space elevators, a space "necklace" around the earth, and tether rescues of stranded astronauts. Several early concepts involving gravity-gradient stabilized tethers are shown in Figure 1. Initial application experiments

for tethered vehicle operations in space began in late 1966 as part of the Gemini program. The effects of firing translational thrusters and the effects of gravity gradient stabilization on the motion of the tethered system were examined using the Gemini XI and XII spacecraft with the spent stage of their Atlas-Agena D launch vehicle.(Lang and Nolting, 1967) Further development of the gravity-gradient concept came in 1969 when A.R. Collar and J.W. Flower proposed a very long tether connecting two satellites - one beyond geostationary altitude and one in low earth orbit, such that the center of gravity was located at geostationary distance.(Collar and Flower, 1969) Additionally, the idea for a space propulsion system was introduced by R.D. Moore, consisting of a conducting wire with plasma contactors at either end. His "geomagnetic thruster" was a true forerunner of present day electrodynamic tethers.(Moore, 1966)

It was not until the early 1970's, however, that coordinated efforts were made to investigate the complex dynamics of long tethers as an innovative approach to space transportation. Mario Grossi's proposal of a shuttle-borne tether for use as an ULF/ELF antenna and radio physics facility was one of the first practical applications study for the use of tethers in space.(Grossi, 1973) Through his involvement in this program, beginning in 1974, Giuseppe Colombo quickly recognized the far-reaching potential of the tether in space transportation.(Colombo et al., 1974) Professor Colombo, who is considered to be the modern pioneer of tethers applications, conceived, introduced or analyzed virtually all of the first space propulsion schemes involving tethers. It was these new methods of generating propulsion through momentum exchange between spacecraft, and in generating electric power and thrust through electrodynamic interactions with the space environment, that established tethers in space as a revolutionary operational capability today. Tether applications in space exist in a wide range of fields, including

aerodynamics, gravity control, electrodynamics, transportation, science studies, and planetary exploration.

B. GRAVITY-GRADIENT STABILIZATION

There are two basic configurations that provide controlled acceleration fields for an orbiting tether system. A gravity-gradient stabilized tether rotates once per orbit in an inertial coordinate frame, while a rotating tether configuration consists of multiple rotations per orbit. An understanding of the basic physical principles behind gravity-gradient forces is fundamental when studying general tether applications. Consider a single satellite in a circular orbit about the earth. It is subject to a gravitational force,

$$F_g = \frac{-GMm}{r^2}$$

where G is the gravitational constant, M is the mass of the earth, m is the mass of the satellite, and r is the radial distance from the center of the earth to the satellite. This force must equal the centripetal force necessary to cause circular motion,

$$F_c = mr\omega^2$$

where ω is the satellite's orbital angular velocity. The balance between the force of gravity, which pulls the satellite towards earth, and the outward centrifugal force, keeps the satellite in orbit. To remain in a circular orbit, the net vertical force acting on the satellite must be zero. Thus, by equating the two forces, the constant angular velocity of the satellite as it orbits the earth can be solved for,

$$\omega^2 = \frac{GM}{r^3}$$

Now consider two masses connected by a tether in a circular orbit such that the system is oriented vertically. Gravity, centrifugal force, and atmospheric drag all vary with altitude, thus each body in a tethered system is subject to separate influences. A simple "dumbbell" configuration, shown in Figure 2, will be in an equilibrium state

orbiting the earth as long as the tether remains aligned in the vertical and all parts of the system have the same orbital angular velocity. For this orientation, the sum of the gravitational forces acting over the system must be equal and opposite to the sum of the centrifugal forces acting on the system. Neglecting the tether's weight, the summation of force becomes,

$$\frac{GMm_1}{r_1^2} + \frac{GMm_2}{r_2^2} = m_1r_1\omega^2 + m_2r_2\omega^2$$

From this equation the tethered system's orbital angular velocity can be computed. The gravitational and centrifugal forces acting on the tethered system are equal and balanced at only one place - the system's center of gravity. This equilibrium point is in a zero-g condition and experiences no net force in the radial direction. It is in free fall as it orbits the earth, but the two end masses are not. They are constrained by the tether to orbit with the same angular velocity as the center of gravity. The value of the orbital radius for the center of gravity is given by,

$$r_0^3 = \frac{GM}{\omega^2}$$

For short tethers, this value will be nearly equal to the position of the center of mass of the system. However, since gravitational acceleration changes non-linearly with distance from the center of the earth, the center of gravity of the tethered system does not necessarily coincide with the center of mass. The separation is not dramatic for systems using short tether lengths, but can be significant for long tethered systems.(Arnold, 1987)

Without the connecting tether, the higher mass would tend to move at a slower orbital velocity, while the lower mass would tend to move at a greater orbital velocity. Thus, the presence of the tether speeds up the higher mass and slows down the lower mass. This causes the higher mass to be subject to a larger centrifugal than gravitational force, and the lower mass to be subject to a larger gravitational than centrifugal force.

With a tether in place, the net effect of these unbalanced forces is to create tension in the tether. The resulting upward acceleration of the higher mass and downward acceleration of the lower mass gives rise to a force couple applied to the system, which forces it into a vertical orientation. Should a disturbing torque act on the tethered system and displace it from the vertical position, this force couple produces restoring forces at each mass, illustrated in Figure 3, which act to return the system to a vertical orientation. These restoring torques act in both in-plane and out-of-plane directions to tend to keep the system in its equilibrium state.

Although this vertical orientation is a stable one, there are weak but persistent forces which cause the tethered system to oscillate about the vertical. These forces include atmospheric drag, solar heating effects, electrodynamic forces (for conducting tethers), solar pressure torque, and geomagnetic torques. For short tether lengths, where the gravity-gradient is relatively constant, the libration frequencies are independent of tether length due to the fact that both the displacement and the restoring forces on the system vary linearly with tether length. This is not the case for very long tethers, however, since the gravity-gradient can vary significantly over the length of the tether. The natural restoring torque for out-of-plane disturbances tends to be stronger than that for in-plane disturbances, thus out-of-plane librations have a higher frequency than in-plane librations. The natural frequency for in-plane oscillations is given by,

$$f = 2\omega$$

For out-of-plane oscillations,

$$f = \sqrt{3}\omega$$

where ω is the orbital angular velocity of the center of mass.

Optimum design considerations for tethers used in space call for minimizing the tether's mass while maintaining its required strength. This is accomplished by using

materials such as aluminum wire and Teflon insulation which have high strength to weight ratios. Additionally, aluminum's conductivity per mass is about twice that of copper, and Teflon provides good resistance to atomic oxygen erosion. The tether cannot be too thin because of the significant risk of being cut by a micrometeorite impact. Collisions with orbital debris pose a threat to any deployed tether, since any such encounter with particles or objects of more than a few grams will almost certainly sever it. The tether must be constructed to survive most impacts so as to have a reasonable expected lifetime. Tethers designed with a constant cross-sectional area have a limited length, however, tethers tapered to maintain a constant stress per unit cross sectional area can theoretically have unlimited length. Thus the optimum design for high tether tensions would be an exponentially tapered tether with a maximum area at the center of gravity and minima at the end masses. Although there is no limit to the length that can be achieved, the payload that can be supported at the ends keeps getting smaller.(NASA Report, 1989)

C. ELECTRODYNAMIC TETHERS

One of the most rewarding applications of tethers to enhance man's use of space may be the electrodynamic tether, a satellite system in which two separate payloads are connected with an insulated conductive wire. Electrodynamic tethers make use of the interactions between a moving conductor, the earth's magnetic field, and the ambient plasma in the ionosphere to allow propulsion and power generation. Such a system could be used with solar arrays to offset drag in LEO, replace batteries for power storage, or provide propulsion for orbital maneuvers.

Consider the ionospheric plasma, co-rotating with the Earth, relative to which a tether is moving with orbital velocity v . For most tether applications v is Eastward, while

the earth's magnetic field B , acts Northward. This produces an induced electric field acting upward, causing a sizable potential difference across the conducting tether due to its motion through the geomagnetic field. By providing contactors (devices capable of passing sufficient current to and from the plasma with little voltage drop) at both ends of the tether, electrical contact with the Earth's LEO plasma environment is made, establishing a current loop through the tether, external plasma, and lower ionosphere. In the undriven state, electrons from the ambient plasma are collected by the upper end of the tether and emitted from the lower end, creating a net positive charge cloud at the top end and a net negative charge cloud at the bottom end. In a quasi-static model, excess free charges are constrained to move along the geomagnetic field lines intercepted by the ends of the tether until they reach the E region of the lower atmosphere where their are sufficient collisions with neutral particles to allow the electrons to migrate across the field lines and complete the circuit. Taking satellite motion into account, however, one finds that by the time the circuit "closes", the satellite has traveled many kilometers. Thus the true dynamic problem appears to be a complex one. Figures 4 and 5 illustrate how current flowing along the wire due to the potential difference is coupled into and through the ambient ionospheric plasma.(Bainum et al., 1986)

There are three basic plasma contactor configurations to provide electrical closure to the space environment. The first consists of passive large area conductors at both ends of the tether. The upper conductor collects electrons, while the lower plasma contactor utilizes its large surface area to collect ions. A large conducting balloon could be used at the upper end in this configuration, with the conductive surface of the spacecraft serving at the lower end.

An alternate method of current coupling consists of a passive large area conductor at the positive end of the tether, and an electron gun at the negative end. In this case, the

ejection of a negative electron at a high energy is the equivalent to collecting a positive ion current. While this configuration allows higher currents to be achieved, it also requires an on-board electrical power supply to drive the electron gun. One general problem with electron guns, is that they tend to become current limited, typically by space charge effects.

The final configuration consists of a plasma-generating hollow cathode assembly at each tether end. Instead of relying on a passive and physically large conducting surface to collect currents, hollow cathodes generate an expanding cloud of highly conductive plasma. This plasma provides the necessary thermal electron density to carry the full tether current in either direction from a tether end, until it is merged into the ambient ionospheric plasma currents. Although this configuration also requires an on-board power supply, the bipolar nature of the emitted plasma offers greater flexibility and has been demonstrated to work.(Olsen, 1981)

Hollow cathode systems are considered to be the most desirable contactor configuration. Their current reversibility allows the tether to function alternately as either a generator or a motor. Additionally, they operate at lower voltages while still producing the desired electrical power levels. They are safer for the spacecraft system because they establish a vehicle ground reference potential with respect to the local plasma. Finally, with hollow cathode contactors, shorter tethers may be used for required current levels, greatly reducing the size requirements for stabilizing end masses, and simplifying tether deployment and dynamics.(NASA Report, 1989)

Tethered systems in LEO generate electrical power at a rate equal to the loss in spacecraft orbital energy due to drag forces. Consider a vertical, gravity-gradient stabilized, insulated, conducting tether, terminated at both ends by hollow cathode plasma contactors. As this system orbits the earth, it cuts across the geomagnetic field lines at

orbital velocities of about eight kilometers per second. A Faraday electromotive potential (emf) is induced in an element of the length of the tether, given by the equation:

$$d\Phi = (\vec{v} \times \vec{B}) \cdot d\vec{l}$$

where $d\Phi$ is the induced emf across the tether element length, v is the tether velocity relative to the geomagnetic field, B is the magnetic field strength, and dl is a differential element of the tether length pointing in the direction of current flow. This emf creates a potential difference across the tether by making the upper end of the tether positive with respect to the lower end, allowing current to flow through the wire. By using variable resistance or impedance matching techniques, the current passing through the tether can be controlled, providing power for on-board systems, as shown in Figure 6.

When the current generated by the induced emf is allowed to flow, a force is exerted on the current, and thus on the tether, by the geomagnetic field given by:

$$d\vec{F} = I d\vec{l} \times \vec{B}$$

where dF is the force exerted on an element of the tether by the magnetic field, I is the tether current, dl is a differential element of tether length pointing in the direction of positive current flow, and B is the magnetic field strength. In LEO, where the relative velocity between the orbiting tether and the rotating geomagnetic field is large, this force is a drag on the tether. A direct result is that when electrical power is generated by the system for on-board use, it is generated at the expense of orbital energy. If the tether is to maintain its altitude, this electrodynamic braking must be compensated for by rockets or other propulsion means.

Alternately, when a current from an on-board power supply is fed into the tether against the emf induced by the geomagnetic field, the direction of the force is reversed and it becomes a propulsive force acting on the tethered system. Figure 7 illustrates this principle, which allows the tether can be used as an electrodynamic thruster, with

applications of orbital maneuvering and drag compensation. The price to be paid in this instance is that the propulsive force is generated at the expense of on-board electrical power.

Electrodynamic tethers also have applications in power storage. Using solar arrays, current could be fed into a tether during periods of array illumination, providing a propulsive force to boost orbital altitude. Then, during periods of darkness, orbital energy could be traded for useful DC electrical power as the geomagnetic field induced voltages across the tether, inducing current flow in the opposite direction. This reversible energy storage system would complement systems employing the charging and discharging of batteries. By itself, however, it is not mass-competitive with conventional battery systems.(NASA Report, 1989)

Thus the electrodynamic tether system presents a new form of continuous power or thrust generation in space, which can in theory produce either an efficient power supply of a few to hundreds of kilowatts of usable electricity, or provide orbital maneuvering forces for the satellite. There are effects due to orbit altitude and inclination which act to limit the effective operating range of the electrodynamic tether system to orbit altitudes of less than 2000 kilometers and orbit inclinations below sixty degrees. The major cause for the altitude effect is the decrease in geomagnetic field strength which goes as the inverse of the third power of the orbit radius. A smaller cause is the orbit velocity of the system which decreases as the inverse square root of the orbit radius. As the orbit inclination is increased, the angle between the orbit velocity vector and the magnetic field vector is decreased until at a polar orbit velocity is parallel to the field. At this point the vector cross product goes to zero and no voltage is induced in the tether. Thus equatorial and low inclination orbits generate the highest emfs since it is here the tether velocity and magnetic field lines are perpendicular.

Other critical issues that affect the performance of an electrodynamic tether include plasma contactor cloud instabilities which impede the current closure process, as well as the characterization of the magnetosphere current closure path and its potential losses. The tether's susceptibility to micrometeoroid/debris damage and the effects of long-term insulator exposure also play a role. And finally, long tether dynamics and associated librations will continually affect the performance of the tether.(Bainum et al., 1986)

III. THE SPACE ENVIRONMENT

A. EARTH'S GEOMAGNETIC FIELD

The magnetic field of the Earth is, to a first approximation, that of a sphere uniformly magnetized in the direction of a centered dipole axis. Both the magnitude and the orientation of this dipole undergo slow time variations, with a time scale of the order of months to years, which give rise to gradual changes of the geomagnetic field components. The "best fit" for this equivalent dipole model, for the smallest cumulative error when compared to the actual field of the Earth, is obtained by an offset of 436 km from the center of the Earth, displaced towards the Pacific ocean. This displaced dipole model, shown in Figure 8, is known as the Eccentric Dipole Model, and describes the measured geomagnetic field to an accuracy of two to three percent. The geomagnetic poles of the dipole, the location where the axis of the fictitious dipole magnet intersect the surface of the Earth, are located about 800 miles from the geographic poles, producing a tilt angle with respect to the Earth's rotation axis of 11.3 degrees. The north geomagnetic pole is located near Thule, Greenland at 78.3N 291.0E. The geomagnetic south pole is located near Volstok Station, Antarctica, at 78.3S 111E. One may accordingly define a geomagnetic equator as the great circle 90 degrees away from either pole in geomagnetic latitude.(Heinz and Olsen, 1993)

The relationships between the geomagnetic latitude and longitude (λ, Λ), and the corresponding geographic coordinates (θ_0, ϕ_0) are given by the equations,

$$\sin \lambda = \cos 78.3^\circ \cos \theta_0 \cos(\phi_0 - 291^\circ) + \sin 78.3^\circ \sin \theta_0$$
$$\cos \Lambda = \frac{\sin 78.3^\circ \cos \theta_0 \cos(\phi_0 - 291^\circ) - \cos 78.3^\circ \sin \theta_0}{\cos \lambda}$$

A static dipole field can be defined by three components. With the radial, tangential and azimuthal components of the dipole field the magnitude and direction of the geomagnetic field vector can be obtained in spherical coordinates. The radial component of the field is given by,

$$B_r = \frac{2B_0 \cos\theta}{(r/R_E)^3}$$

The field's tangential component is given by,

$$B_\theta = \frac{B_0 \sin\theta}{(r/R_E)^3}$$

The component of the field in the azimuthal direction is,

$$B_\phi = 0$$

Figure 9 depicts the coordinate system for the magnetic dipole field, where r is the distance from the dipole to the fieldpoint, R_E is the radius of the Earth, θ is the co-latitude of the fieldpoint, ϕ is the azimuthal angle, and B_0 is the surface field at the geomagnetic equator. (Tascione, 1988)

An equation for an individual field line may be obtained by setting,

$$\frac{dr}{rd\theta} = \frac{B_r}{B_\theta}$$

which has the solution,

$$r = R_0 \sin^2 \theta$$

where R_0 is the radial distance of the equatorial crossing of the magnetic field line. This equation, its geometry depicted in Figure 10, may be rewritten in terms of geomagnetic latitude, the compliment of co-latitude,

$$r = R_0 \cos^2 \lambda$$

The inclination of the field line, called the magnetic dip angle, is related to magnetic latitude by the equation,

$$I = \arctan(2 \tan \lambda)$$

Finally, the magnitude of the field at any given point is obtained from solving the equation,

$$B = \frac{B_0}{(r/R_E)^3} (3 \sin^2 \lambda + 1)^{1/2}$$

B. IONOSPHERIC PLASMA

More than 99 percent of matter in the universe exists in the plasma state, a mixture of ionized and electrically neutral gases. A gas can be both ionized and electrically neutral at the same time, provided there are as many free electrons in the gas as there are net positive charges on the positive gas ions. Thus, plasma consists of a homogeneous mixture of electrons and positive ions, surging and swirling in electromagnetic bondage. This plasma becomes important in the Earth's environment in the ionosphere, which extends upward from about fifty kilometers above the ground to about 1000 kilometers in altitude, and it is sustained by the ionizing action of solar ultraviolet and x-ray radiation on the neutral atmospheric gas. Between these altitudes, ions and electrons are present in sufficient quantities to affect the propagation of radio waves at frequencies from a few Hertz up to several megahertz. (Heinz and Olsen, 1993)

The variation of electron density with altitude led to the subdivision of the ionosphere into distinctive layers - the D, E and F regions shown in Figure 11. Ionospheric plasma is very tenuous, and is not predominantly composed of charged particles. Even at the most dense layers of the ionosphere, there are rarely more than one million electron-ion pairs in a cubic centimeter (cc) of space. In comparison, the neutral gas density for the same region is typically one billion particles per cc. Nevertheless, the positive ions and electrons are present in sufficient numbers in the ionosphere to reflect radio waves back to earth, and it was through this process that ground-based radio wave

observations first detected the region of plasma above the Earth's electrically neutral atmosphere.(NASA Report, 1993)

On the surface of the earth and upward for approximately fifty kilometers, the atmosphere can be considered to be an electrical insulator, and therefore there are no currents flowing in that region. However, convective movements of the conducting upper atmosphere across the earth's magnetic field lines produce electric currents in the ionosphere. In addition to natural variations in this plasma environment, satellites can alter the space plasma as they pass through their orbits. An important scientific objective of the study of tethers in space, involves measuring the plasma and magnetic field environment of an electrodynamic tether. VHF radar observations of the space environment can be made in an effort to characterize the environment before and after the satellite passes through the radar beam. These observations can be used to identify interactions between the tethered electrodynamic satellite system and the plasma.

Some special features are likely to develop in the vicinity of a tether as it actively perturbs the plasma. Traveling at orbital velocities, the satellite affects the density, temperature, and electrical properties of the surrounding plasma. A plasma sheath develops around the satellite, while a wake, in some respects resembling a wake left by a boat in the water, trails behind. Due to long range interactions between charges, a plasma can sustain cooperative phenomena such as waves or oscillations down to much lower densities, and over far greater distances than ordinary gases. The plasma sheath around the satellite is predicted to be unstable and to change in size and shape with variations in ionospheric density, magnetic field alignment, and the voltage developed across the tether. These changes affect the type and amplitude of waves excited in the wake, creating observable turbulent disturbances in the environment around the satellite.(NASA Report, 1993)

IV. THE PMG EXPERIMENT

A. MISSION OBJECTIVES

NASA's Plasma Motor Generator (PMG) mission was an active space experiment conducted in Low Earth Orbit (LEO), designed to validate theoretical predictions that a plasma discharge from an onboard hollow cathode assembly (HCA) would provide a low impedance electrical coupling between an orbiting spacecraft and the ambient ionosphere for bipolar charge transfer. In addition to the demonstration of plasma contactor performance was an investigation of electrodynamic-tether behavior functioning as either an orbit-boosting electrical motor, or as a generator that converts orbital energy into electricity. (Jost and Stanley, 1994)

A comprehensive set of ground-based measurements, utilizing several globally-distributed ground stations, was defined to provide an evaluation of the interactions between the operational PMG system and the LEO environment. Sixteen fixed and transportable radar, magnetometer, and optical systems were used for remote measurements in support of the mission science objectives. This multi-sensor approach was used to study large-scale geophysical interactions between the orbiter and the ambient environment, monitor spacecraft/tether dynamics, and provide general orbital tracking records. Analysis of these remote measurements provided details on the following mission performance objectives (Jost and Stanley, 1994):

- Far End Package (FEP) deployment to greater than 200 meters
- Tether deployment dynamics and damping
- Space-based hollow cathode plasma production operation
- Current flow along geomagnetic field lines, and closure through the ionosphere
- Tether deflection by $I \times B$ drag and thrust forces

B. PHYSICAL DESCRIPTION

The experiment consisted of a tethered system of two identical plasma contactors connected via an 18-AWG 500 meter conducting tether. Experiment flight hardware included four major subsystems; the Far End Package (FEP), Near End Package (NEP), an electronics box, and a Plasma Diagnostics Package (PDP). The two-body tethered satellite system was stabilized in a gravity-gradient configuration, with the FEP oriented away from earth following its spring-ejection from the second stage of the DELTA-II. The FEP housed a hollow cathode-based plasma contactor inside an open metal box of dimensions 0.3m x 0.3m x 0.3m. The NEP, consisting of the electronics box and another plasma contactor, remained fixed to the second stage of the Delta II. The PDP was also attached to the rocket body, and consisted of two detectors, the Small Electron Electrostatic Analyzer (SESA) and the Ion Mass and Energy Analyzer (MESA). (Lilley et al., 1994)

In addition to the $\vec{v} \times \vec{B}$ induced potential difference along the tether, batteries were used to bias the NEP and FEP with respect to each other. Varying resistive loads, in series with the tether, were cycled through during the experiment. The resulting current through the tether was the net effect of both contactor plasma clouds, one collecting and the other emitting electron current to the local space plasma environment. When electrons were collected at the FEP, the PMG system was in the Motor mode. (Figure 7) When electrons are collected at the NEP and by the Delta II rocket body, the system was in the Generator mode. (Figure 6) The limiting factor of this electrical circuit is the ionosphere's ability to carry current. For this reason, plasma contactors must effectively spread the currents over a large enough area to reduce the current densities to the necessary levels. Thus, plasma contactors at each end of the electrodynamic tether

collection and emission by neutralizing space charge and scattering electrons across the geomagnetic field lines.(Jost and Stanley, 1994)

Plasma contactors are a promising technology with applications in electrodynamic tether systems as well as grounding spacecraft to the space plasma environment. A hollow cathode based plasma contactor is a device that emits a dense, low-temperature plasma cloud through which ions and electrons are emitted and electrons are collected from the surrounding plasma. The construction of the hollow cathode assembly (HCA) used aboard PMG is illustrated in Figure 12. Functionally, the HCA heats a flow of xenon gas to relatively high temperatures (typically 1100° C) within a hollow electron-emitter (barium-oxide impregnated tungsten) cathode in the presence of a strong voltage gradient between the cathode and a corresponding anode plate. In this condition, the partially ionized gas establishes a highly-ionized "plasma-discharge," which allows current to flow freely between cathode element and an external anode, in this case the LEO ionosphere.(Jost and Stanley, 1994)

In electron emission mode, the electrons from the plasma contactor carry the current while the ions neutralize the electron's space charge. In the dense contactor plasma, the electron density is approximately equal to the ion density. Higher energy electrons stream through the slowly expanding ion cloud while the lower energy electrons are trapped within the cloud by the potential distribution near the cathode. Each outgoing ion allows a number of electrons to be emitted, at roughly a ratio which is,

$$\frac{n_e}{n_i} \approx \sqrt{\frac{m_i}{m_e}}$$

When the plasma contactor is collecting electrons, the contactor ions once again neutralize the space charge of the ambient electrons. The contactor plasma is extremely turbulent due to current driven electrostatic instabilities. Incoming electrons are scattered

by the contactor plasma and can be collected across the geomagnetic field lines within an effective radius of several meters.(Lilley et al., 1994)

C. FLIGHT PROFILE

The experiment duration, in terms of plasma contactor operation and consequential active environment interaction, extended six to seven hours (approximately four orbits) until the NEP and FEP batteries expired. As a result of the successful activation and extended plasma contactor operations, the ground sites typically had opportunities to collect data during at least three passes. Figures 13 and 14 show the mission flight profile and the relative positions of the four ionospheric radars used to view the PMG geomagnetic flux-tubes.(Jost and Stanley, 1994)

D. RADAR OBSERVATION SITES

The VHF radar technique utilized for PMG has been demonstrated during several spaceborne particle beam and plasma source experiments including NASA CHARGE-II, SDIO SPEAR I, NASA ATLAS, and the Soviet-French ARAKS series. Beam steering monostatic (MST) doppler radars measure the doppler shift of oblique backscattered echoes resulting from the ubiquitous small-scale turbulence in the atmosphere. These phase coherent radars allow measurement of the amplitude and doppler velocity in the direction of probing of radio waves that are scattered back to the receiving antennas.

Explaining MST radar observations requires two basic echoing mechanisms, namely scattering and reflection. For monostatic radars, backscatter and reflection arise from the variation of the refractive index, n , whose spatial scale along the axis of the radar beam is half the radar wavelength. For a near vertical beam at fifty megahertz, observed echoes are usually a combination of Bragg scatter (also called turbulent scatter),

Fresnel scatter, and Fresnel reflection. The major process causing the echoes of MST radars from the ionosphere is the scattering and reflection from refractive index irregularities due to temperature, humidity and electron density fluctuations. In addition, observable radar echoes from meteor trails and incoherent scatter from free electrons in the ionosphere should frequently occur.(Liu and Edwards, 1989)

When a radio wave traveling at an angle to the magnetic field encounters a field-aligned disturbance, it is scattered such that its angle of incidence equals its angle of reflection. For the case when the wave is normal to the disturbance, the angle between the incident and reflected waves is 180 degrees and the wave backscatters. Thus a radar pointed such that it has a line of sight that is normal to the field lines will detect a maximum strength backscatter signal from any waves propagating along the field lines. The refractive bending of radar waves in the VHF frequencies is small enough that the ray paths can be approximated by straight lines.(Liu and Edwards, 1989)

Observations of the spacecraft/environment interactions were to be obtained from a ground-based sensor network during the PMG mission. Scattering from refractive index variations caused by ionospheric plasma irregularities was expected. The interaction of the plasma clouds, produced by the HCA's, with the ionosphere was expected to cause turbulent ambient-plasma electron distributions detectable with ground-based VHF radar. Similarly, the refractive index of the plasma surrounding the operating PMG plasma source should have been overdense relative to incoming VHF electromagnetic waves, causing the apparent vehicle radar cross section to be evident in the collected radar data. Thus, two primary measurable characteristics of the PMG plasma clouds were expected:

- Enhanced ionization levels and plasma turbulence in the vicinity of the vehicle during contactor operation.

- Propagation of plasma turbulence along geomagnetic flux lines over long distances (100's of kilometers).(Jost and Stanley, 1994)

Four medium and large power-aperture VHF radar systems were utilized in support of the PMG mission, located in relative positions for favorable viewing of the geomagnetic flux-tubes for the first four, active-orbit ground tracks of the mission. All four systems operated in a pulsed, narrow-band, fixed-pointing configuration with a center frequency of approximately fifty megahertz. The powerful ionospheric radar at Jicamarca Radio Observatory in Lima, Peru (11.948 S, 76.872 W) was activated to observe spacecraft/environment interactions, and provide data on plasma contactor operation, plasma cloud size and diffusion properties, and geomagnetic field propagation effects. NASA/JSC deployed a transportable radar to the island of Hawaii (19.514 N, 151.849 W) for direct observations of PMG plasma clouds, providing data complementary to Jicamarca. In addition, two wind-profilers, the NOAA VHF Radar Facility in Piura, Peru (5.167 S, 80.617 W) and the NOAA VHF Radar Facility on Pohnpei Island, Micronesia (6.96 N, 158.19 E) were configured for ionospheric measurements, supporting the Hawaii measurements, and providing a measure of turbulence propagated along the geomagnetic field. Finally, the USSPACECOM Radar Tracking network and the Kwajalein Missile Range provided precision orbital tracking of the tethered system during the course of the experiment.(Jost and Stanley, 1994)

The primary goal for all the VHF radar sites was observation of plasma-perturbation signatures caused by PMG moving through the lower ionosphere. Based on the high scattering cross sections of field aligned ionospheric plasma turbulence, for electromagnetic radiation in the VHF bands, it was possible to observe the space-environmental effects of field-aligned disturbances projected great distances along the geomagnetic field lines. Observation of such disturbances supports the concept of coupled electrical current, flowing from within the conducting tether wire into the

rarefied ionospheric plasma. These traveling waves are theorized to stay tightly confined to the geomagnetic field lines until the ambient density and collision frequencies are high enough (at low altitudes) to allow cross-field diffusion and closure of the electrical circuit.(Jost and Stanley, 1994)

V. EXPERIMENTAL OBSERVATIONS AND ANALYSIS

A. HAWAII PASSES

The Transportable Radar System (TRS) deployed to Hawaii for ionospheric observations was a medium power-aperture coherent detection system consisting of several transmitter modules, two coherent multi-channel receivers, and several phased-array antenna systems that allowed tailoring for particular radiation pattern configurations. Electronic beam steering was incorporated into the design which enabled the radar to switch rapidly between direct illumination of the predicted PMG position in its orbit, and specular viewing of the projected geomagnetic lines which mapped from the orbiter. In this way, antenna pointing was optimized for each observation period to investigate the characteristics of field-aligned plasma turbulence propagating away from the active PMG tether-system along the geomagnetic flux tubes.

The monostatic RX/TX phased array was capable of generating a peak power of 160 kilowatts with a duty cycle of one percent at its operating frequency of fifty megahertz. An additional monopulse RX array was configured to provide interferometry measurements. The antenna configuration provided a gain of twenty-six decibels and was aimed in azimuth at the geomagnetic north pole, which for the Hawaii location was eleven degrees east of geographic north. It was phased in the vertical direction to produce the required elevation angle for the planned ionospheric observations. In its first pass over Hawaii, PMG was expected to pass through the radar's field-of-view at an elevation angle of thirty-seven degrees. Subsequent observations perpendicular to the magnetic field lines over Hawaii were made at an elevation angle of fifty-five degrees.(Figure 15) The radar's vertical and horizontal beamwidths were twenty degrees and five degrees respectfully.

Electromagnetic energy with a pulse width of fifty microseconds was sent out every interpulse period (IPP). For the first pass of PMG over Hawaii, an IPP of five milliseconds was used. Following each transmission, the receivers were used to detect any incoming fifty megahertz radiation. Sampling every forty microseconds resulted in a range gate interval of 6000 meters. Due to the long slant ranges to the satellite, a coded waveform would be required to negate the effects of range-aliasing, while ensuring adequate doppler coverage, and sufficient average radiated power. However, a coded pulse was not used, and thus returns from two six kilometer intervals, separated by 750 kilometers, are actually contained in each sampled gate. A total of 48 range gates were sampled, beginning at a slant range from the radar of 107 kilometers for PMG's first pass over Hawaii.

At the Hawaii radar site, the in-phase and quadrature components of the received radar signal from each scattering volume were recorded continuously on analog tape. The vast majority of what the receivers detected was white noise background. However, if any turbulent propagations were present in the observed region of the ionosphere, such as those caused by meteor trails, then an enhancement of the incoming fifty megahertz radiation could be detected at a specified time delay after the initial pulse. The line of sight range from the radar to the returned signal could then be determined by the time delay between the transmitted and received signal.

The Hawaii data underwent the first phase of processing at Systems Planning Corporation - Center for Space Physics in Houston, Texas. The analog tape was digitally sampled and analyzed, to allow plots of signal intensity as a function of time and range to be prepared. The power representing the signal was determined by summing the squares of the in-phase and quadrature components of the received signal. In order to normalize the received power to the system noise, the signal plus noise power was first calculated,

then the noise power was subtracted from it. Noise estimates were calculated by averaging sampled ranges that did not contain radar echoes, while signal plus noise estimates were calculated by averaging sampled ranges that included returns. Data collected during the first pass of PMG over Hawaii are shown in Figure 16.

At the Naval Postgraduate School, additional analysis of the Hawaii data was performed. The backscattered signals sampled from the forty-eight range gates provided both intensity and doppler frequency information. A fast Fourier transform was used to derive this spectral information for each return echo observed in the Hawaii pass. Interpretation of the collected data was complicated by the background noise of meteor events and unstable E-layer echoes, as well as the ambiguity resulting from the range-aliased waveform. By comparing the spectral components of each observed return, however, discrimination signatures to unambiguously distinguish natural events from PMG-induced echoes were determined. This analysis was performed by Wayne Brewster, as part of his Master's Thesis.(Brewster, 1994) The PMG satellite system was apparently not observed at thirty-seven degrees elevation during its first pass over Hawaii. Halfway through the pass, at time 14:56:00 (HHMMSS), the radar beam was switched to an elevation angle of fifty-five degrees to look perpendicular to the magnetic field lines. Approximately four minutes after the anticipated PMG meridian passage, a cluster of strong echoes were detected at a slant range consistent with that of the ray-path specular point for the geomagnetic flux-tube linked to PMG. The discrimination signatures for these signals were consistent with those determined to be plasma.(Brewster, 1994) Figures 17-19 display the spectral characteristics of these signals, as well as the time and slant range information about the echoes. The top panel of Figure 17 shows the intensity of returns in range gates 1-16. The bottom panel is a fast fourier transform versus time plot of the radar returns for range gate 3, corresponding to slant ranges from 869 to 875

kilometers. Figures 18 and 19 display similar returns for range gates 4, 5, 6, and 7, with each six kilometer interval beginning at a slant range of 875, 881, 887, and 893 kilometers respectively. A disturbance, interpreted as a traveling plasma wave can be identified in these figures. First seen in range gates 3 and 4, the event occurs at approximately time 14:58:26. Six seconds later, in range gates 5, 6, and 7, a disturbance is observed at time 14:58:32.

The Kwajalein Missile Range radar was tracking the orbiting tether system as it passed overhead, recording the slant range, azimuth and elevation of the Delta II in its orbit. From these measurements an accurate orbit was derived, giving the PMG altitude and latitude and longitude as it orbited the earth. Projecting the orbit of PMG experiment forward until it reached Hawaii allowed a precise determination of the time PMG crossed the geomagnetic meridian to be made. Table 1 contains a portion of the orbital data for PMG as it made its first pass over Hawaii. Meridian crossing occurred when the azimuth angle reached eleven degrees, at time 14:54:19 (HHMMSS). At this time PMG was orbiting over the Earth at a geographic latitude of 25.8 degrees north, geographic longitude of 206.5 degrees east, altitude of 641.2 kilometers, and a slant range from the radar site of 982.5 kilometers. PMG was approaching its highest inclination on its ground track at this time, and was decreasing in altitude.

While no direct scatter from the satellite system was observed at the anticipated meridian crossing point during this pass, through reconstruction of tracking radar data, the exact time PMG moved through the center of the beam and crossed the magnetic meridian was established. If the cluster of plasma echoes, subsequently detected with the radar beam perpendicular to the magnetic field, were a result of PMG's passage through the field line, then these signals equate to a turbulent plasma waveform aligned with the magnetic field line intersected by the PMG orbiter, traveling at some propagation

velocity. The velocity of the plasma waveform, in the direction along the magnetic field line, can be calculated using the approximate flux-tube path length from PMG to the radar field-of view perpendicular to the field lines, and the time delay between meridian crossing and the detection of the plasma events.

Using the geographic coordinates of the Hawaii radar site, its magnetic latitude can be calculated to be 20.5 degrees north. Likewise, using the geographic coordinates of the nadir point associated with PMG's meridian crossing, a magnetic latitude of 26.3 degrees north is found. The magnetic dip angle of the field lines at these locations can then be calculated using these magnetic latitudes. Above Hawaii, the field lines are inclined at an angle of approximately thirty-seven degrees, while at the point of meridian crossing this inclination increases to approximately forty-five degrees. Thus, at the point in the ionosphere where the Hawaii radar was pointing perpendicular to the field line, the value of the inclination is between these two angles. Since the inclination of the field line is relatively constant over this region, a straight line approximation will be used for the flux-tube distance between PMG meridian crossing and the field-of-view perpendicular to the field line.

Forming a right triangle from the pass geometry, shown in Figure 20, the approximate propagation distance of the plasma waveform can be calculated by multiplying the slant range to PMG meridian crossing by the sine of the angle between the two radar beam positions. The result is a propagation distance of 303.6 kilometers. The time delay between meridian crossing and detection of the first plasma echo was four minutes and seven seconds. Using this time and distance, a propagation speed of 1.20 kilometers per second can be calculated.

The nominal sources of error in this calculation include the straight line approximation for the geometry of the field line, six second uncertainty in time of

observation of the disturbance, as well as single source projection errors for the orbital position of the Delta II rocket based on radar tracking by Kwajalein.

B. JICAMARCA PASSES

In the foothills of the Andes mountains, the Radio Observatorio de Jicamarca was also employed to measure the intensities of field-aligned propagations. Since Jicamarca is located approximately one degree north of the geomagnetic equator, the local magnetic field lines are near horizontal, presenting an excellent opportunity to observe plasma propagations associated with PMG charge neutralization. With a peak power of two megawatts and a duty cycle of 0.6 percent, this fifty megahertz observatory is the world's largest power-aperture radar. The radar's antenna has a two-way beamwidth of one degree, and provides forty-five decibels of gain. A waveform with a pulse width of 6.67 microseconds and a pulse period of 1100 microseconds was used for the ionospheric observations. Sampling of return echoes was divided into 250 range gates, each with an interval of 500 meters, providing a total window of 125 kilometers for data collection.

Throughout the data acquisition, the Jicamarca radar was pointed perpendicular to the geomagnetic field lines in the lower ionosphere. The real and quadrature outputs of the receivers were digitized and recorded to 8-mm recording tape at the radar site. While this data was not available to the researchers at the Naval Postgraduate School for further processing, the times and ranges of initial A-scope detections of propagating plasma turbulence, similar to those observed in the Hawaii, were recorded and presented in the PMG Mission Report.(Jost and Stanley, 1994) Discrete radar detections were obtained in passes 2, 3, and 4, where strong echo returns from flux-tube heights consistent with PMG were observed.

1. Pass 2

Pass 2 over Jicamarca was a descending pass north of the observatory (i.e., the satellite was moving from northwest to southeast in its groundtrack), with PMG losing altitude in its orbit. The tethered satellite system crossed the Jicamarca magnetic meridian when it reached an azimuth angle of six degrees east of geographic north. From the orbital tracking data in Table 2, this occurred at time 16:57:03 (HHMMSS), when PMG was orbiting over the Earth at a geographic latitude of 7.2 degrees south, geographic longitude of 283.6 degrees east, altitude of 193.2 kilometers, and a slant range from the radar site of 566.7 kilometers. The radar event associated with plasma turbulence projected along the field line that coupled the PMG system and the radar's field-of-view occurred at a time of approximately 17:03:30 (plus or minus thirty seconds), at a slant range of 265.0 kilometers. The geometry associated with these observations is shown in Figure 21.

A slightly different approach in calculating the distance traveled by the propagating plasma wave is used for the Jicamarca passes. Due to the dipole-behavior of the flux-tube geometry, the height above the radar of the field-aligned current flow is dependent on the latitude displacement of PMG from Jicamarca as the tethered satellite system crosses the magnetic meridian. Figure 22 graphs this flux-tube height dependence for a 300 kilometer typical-altitude reference. The height of the field line centered in the radar's beam is found by adding the flux-tube height variation from Figure 22 to the altitude of PMG at meridian crossing.

PMG crossed Jicamarca's magnetic meridian during pass 2 at a time of 16:57:03. From the geographic position of the nadir point, the difference in latitude between meridian crossing and radar location was 4.7 degrees. Figure 22 indicates a flux tube height variation of 365 kilometers using this value. Subtracting out the 300 kilometer

reference height results in the magnetic field line above Jicamarca being sixty-five kilometers higher in altitude than at the point of PMG meridian crossing. The geomagnetic position of the radar site, located one degree north of the magnetic equator, allows the dip angle of the field lines above Jicamarca to be calculated at two degrees. This angle is also equal to the angle off vertical that the radar beam is pointing for perpendicular observation of the field lines overhead .

From Figure 21, the arc length S can be calculated using the latitude difference between Jicamarca and the point of meridian crossing, and the radius from the center of the earth to the altitude at which PMG crossed the field line,

$$S = (4.7^\circ) \left(\frac{\pi}{180} \right) (6378.1 \text{ km} + 193.2 \text{ km}) = 541.5 \text{ km}$$

In order to find the propagation distance D, we must first subtract that part of the arc length calculated above that is swept out due to the inclination angle I of the radar beam, using a radius equal to the height at which PMG crossed the field line,

$$(2^\circ) \left(\frac{\pi}{180} \right) (193.2 \text{ km}) = 6.7 \text{ km}$$

The difference between this two calculations is 534.7 kilometers, which approximates the distance the propagating plasma wave traveled in a horizontal direction along the magnetic field line. By forming a right triangle with this distance as one side, and the sixty-five kilometers traveled in the vertical direction as the other, the value of the hypotenuse describes the approximate total distance traveled by the wave, calculated to be 538.7 kilometers.

The first radar return signals were detected at approximately 17:03:30, six minutes and twenty-seven seconds following PMG meridian crossing. Using this time span and the distance calculated above, an average propagation speed of 1.39 kilometers per second can be found. The thirty second uncertainty in the reported time of observance gives a range from 1.29 to 1.51 kilometers per second.

2. Pass 3

Pass 3 over Jicamarca was also a descending pass, however, this time the satellite system crossed the magnetic meridian south of the observatory, and was gaining altitude in its orbit. Meridian crossing occurred 180 degrees from the Pass 2 location, at an azimuth angle of 186 degrees east of geographic north. From Table 3, this occurred at time 18:38:29 (HHMMSS), when PMG was orbiting over the Earth at a geographic latitude of 17.3 degrees south, geographic longitude of 282.5 degrees east, altitude of 215.0 kilometers, and a slant range from the radar site of 644.1 kilometers. The radar event associated with this pass occurred at a time of approximately 18:48:30 (plus or minus thirty seconds), at a slant range of 240.0 kilometers. Figure 23 illustrates the geometry associated with these observations.

For Pass 3 calculations, the same method utilized in Pass 2 was used. Observe that PMG crossed the magnetic meridian at time 18:38:29. This time, however, PMG passed south of Jicamarca, and from the geographical position of the nadir point, the difference in latitude from the radar site was -5.4 degrees. From Figure 22, this angular difference equates to a flux-tube height variation of twenty-seven kilometers once the 300 kilometer reference altitude is subtracted. Thus the field line rises twenty-seven kilometers from the point at which PMG crosses it to the point located at the center of the radar beam.

With this pass geometry, shown in Figure 23, the desired propagation distance in the horizontal direction is the combination of the arc length S , and the arc length swept out by the inclination angle of the radar beam from local vertical,

$$(5.4^\circ)\left(\frac{\pi}{180}\right)(6378.1 \text{ km} + 215.0 \text{ km}) + (2^\circ)\left(\frac{\pi}{180}\right)(215.0 \text{ km}) = 625.4 \text{ km}$$

Once again forming the right triangle with sides of 625.4 kilometers and twenty-seven kilometers, the hypotenuse describes the approximate total distance of wave propagation. This value calculates to be 626.0 kilometers.

The plasma echoes were reported at time 18:48:30 during this pass, which was ten minutes and one seconds following PMG meridian crossing. This time delay equates to an average propagation speed for this pass of 1.04 kilometers per second. The uncertainty again comes from the reported time of echo activity, resulting in a probable range of 0.99 to 1.10 kilometers per second.

3. Pass 4

Like Pass 3, Pass 4 was also a descending pass south of the observatory, with PMG gaining altitude in its orbit. From Table 4, PMG reached an azimuth angle of 186 degrees at time 20:19:11 (HHMMSS), marking its magnetic meridian crossing. At this time PMG was orbiting over the Earth at a geographic latitude of 23.7 degrees south, geographic longitude of 281.9 degrees east, altitude of 282.8 kilometers, and a slant range from the radar site of 1365.1 kilometers. As with the previous passes, strong radar returns were observed, occurring at a time of approximately 20:42:30 (plus or minus thirty seconds), at a slant range of 445.0 kilometers. Figure 23 again illustrates the geometry associated with these observations.

Pass 4 calculations are very similar to Pass 3, however, PMG crossed the meridian much further south in this case. At time 20:19:11, orbital tracking data shows that PMG crossed Jicamarca's magnetic meridian. The geographic latitude associated with the nadir point of this crossing differed from the radar position by -11.8 degrees. Entering Figure 22 with this value results in a flux-tube height variation of approximately 181 kilometers, once the 300 kilometer reference height is subtracted. This is the vertical

distance the plasma waveform transited from the meridian crossing point before passing through the radar beam.

The horizontal propagation distance is calculated as for Pass 3, the combination of two arc lengths,

$$(11.8^\circ)\left(\frac{\pi}{180}\right)(6378.1 \text{ km} + 282.8 \text{ km}) + (2^\circ)\left(\frac{\pi}{180}\right)(282.8 \text{ km}) = 1378.2 \text{ km}$$

Thus, the right triangle for this pass geometry has sides of 1378.2 kilometers and 181 kilometers, resulting in a total propagation distance of approximately 1390.0 kilometers.

The radar event associated with this pass occurred at time 20:42:30, twenty-three minutes and nineteen seconds following meridian crossing. This equates to an average propagation speed of 0.99 kilometers per second. The thirty second uncertainty in detection of the event results in a probable range of 0.97 to 1.02 kilometers per second.

VI. SUMMARY AND DISCUSSION

The two-body tethered satellite system that comprised NASA's PMG experiment was stabilized in a gravity-gradient configuration, with hollow cathode plasma sources at either end of a 500 meter conducting wire. These hollow cathode plasma contactors coupled electric currents from the wire directly into the ambient ionospheric plasma, providing an excellent opportunity to observe the ionospheric modification effects, turbulent signatures, and spacecraft-environment interactions of an orbiting plasma generator.

At any given time, the hollow cathodes at either end of the tethered satellite system apply potential pulses of opposite polarization to the magnetic flux tubes they intercept. The perturbation that occurs as a result of this charge transfer generates plasma waves which travel away from the PMG system, transporting the space charge set up between the tether end flux tubes. These turbulent plasma waveforms, triggered by the conducting tether and plasma contactors traversing the earth's geomagnetic field lines in the ionosphere, appear to travel tightly confined along the field lines over very large distances. Due to the excellent scattering properties of ionospheric plasma irregularities, these traveling waveforms are detectable from ground-based radar.

Through range probing of the geomagnetic flux-tubes above several VHF radar sites, field-aligned disturbances of a propagating plasma structure associated with PMG was observed on several of the spacecraft's passes. Strong, persistent echo returns from the predicted flux-tube heights were observed, which mapped back to PMG at the time of meridian crossing with an average velocity corresponding to average ion velocities in the lower ionosphere. The following table summarizes the results obtained during the PMG experiment, from observations made in Hawaii and Jicamarca,

Site	Pass	Meridian Crossing (HHMMSS)	Radar Event (HHMMSS)	Time Delay (SEC)	Propagation Distance (KM)	Effective Speed (KM/SEC)
HI	1	14:54:19	14:58:29	247	303.6	1.20
JIC	2	16:57:03	17:03:30	387	538.7	1.39
JIC	3	18:38:29	18:48:30	601	626.0	1.04
JIC	4	20:19:11	20:42:30	1399	1390.0	0.99

The observation of two distinct signals during the Hawaii pass remains an unsolved problem. Perhaps a small component of the wave's velocity in the radial direction causes the echoes to be observed at the two specified times. Notice also that some diffusion or eddy motion occurs over the large distances of observation involved in this experiment, seen by the decreasing waveform propagation speeds in the successive Jicamarca passes as the propagation distances increased.

In comparison to the average propagation velocities shown in the table above, the thermal velocity of the ionosphere electrons is given by the equation,

$$v_{th} = \left(\frac{kT_e}{m_e} \right)^{1/2}$$

where k is Boltzmann's constant ($1.38 \times 10^{-23} \text{ J / } ^\circ \text{ K}$), T_e is the average temperature of the electrons (use 1000° K), and m_e is the electron mass ($9.1 \times 10^{-31} \text{ kg}$). Calculating this value results in an electron thermal velocity of approximately 123 kilometers per second - much greater than the observed velocities above. Assuming the thermal temperature of the ions is the same as the electrons, and substituting the oxygen ion atomic weight (15.999) into the above equation, the ion thermal velocity can be calculated to be approximately 0.72 kilometers per second. This value is of the same order as the

propagation velocities observed in the table above. Since the hollow cathode plasma sources were emitting xenon gas, this calculation is repeated using xenon ions (atomic weight of 131.30). The resulting xenon ion thermal velocity is 0.25 kilometers per second, which is close to an order of magnitude less than the values in the table.

Plasma waves propagating away from an electrodynamic tether system in low-earth orbit have been postulated to be Alfvén and fast-mode waves. Alfvén wave dispersion can be thought of as representing the wave that propagates when a field line, loaded with plasma, is plucked in the transverse direction. Such waves travel tightly confined to the Earth’s magnetic field lines, and possible reflection of these waves may occur at density gradients like the E-layer of the Earth’s ionosphere.(Dobrowolny, 1993) The Alfvén velocity is given by the equation,

$$v_A = \frac{B_o}{(\mu_o \rho_m)^{1/2}}$$

where μ_o is the permeability constant ($4\pi \times 10^{-7} H/m$), $\rho_m = n_o m_i$ is the ion mass density, and the measured value of the Earth’s magnetic field at the Earth’s surface at the equator is $B_o = 3.13 \times 10^{-5} T$. Using a value for the ionospheric number density of $n_o = 10^{11} m^{-3}$ and assuming oxygen ions, the resulting Alfvén velocity is 540 kilometers per second. Repeating the calculation for xenon ions results in an Alfvén velocity of 189 kilometers per second. Neither of these results are of the same order as the observed propagation velocities above Hawaii and Jicamarca.

Following the results of Urrutia et al., 1994, it may be that these plasma disturbances propagate in a whistler mode. These results differ fundamentally from the

traditional current model: instead of Alfvén wings and a phantom current loop, Urrutia predicts whistler wings and a short diffuse current loop, due to cross-field shunting electron Hall currents. At each position in their orbit, the plasma contactors on the electrodynamic tether excite a low-frequency whistler wave packet along the magnetic field line. The superposition of these wave packets forms a coherent, wing-like current structure propagating away from the tether system, which travel along the field lines at whistler speeds and disperse by inducing secondary plasma currents. The results of this study suggest that an electrodynamic tether cannot generate a long, filamentary current loop. Instead, the current loop is shunted by cross field currents associated with the continuous shedding of whistler waves, well before encountering the boundary of the plasma. Such a whistler wing generated by a long space tether could possibly produce a whistler tone detectable at the ground when the tether passes by. (Urrutia et al., 1994)

In order to find the phase velocity of a whistler wave traveling through the ionosphere, it is necessary to first solve for the refractive index of the ambient plasma. This refractive index, n , can be found from the following equation,

$$n^2 = 1 - \frac{\omega_p^2 / \omega^2}{1 - \omega_c / \omega}$$

where ω is the frequency of the wave, the plasma frequency, ω_p , is given by the equation,

$$\omega_p^2 = \frac{n_o e^2}{\epsilon_o m_e}$$

and the electron gyrofrequency, ω_c , is given by the equation,

$$\omega_c = \frac{qB}{m_e}$$

For these equations, n_o is the ionosphere number density, e is the electron charge ($1.6 \times 10^{-19} C$), ϵ_o is the permittivity constant ($8.85 \times 10^{-12} F / m$), m_e is the electron mass, q is the charge on the particle - in this case an electron, and B is the strength of the magnetic field (use B_o). Calculating the plasma frequency and the electron gyrofrequency using these numbers results in values of 2.84 megahertz and 0.88 megahertz, respectively. For the special case of whistler wings, where $\omega \ll \omega_c$, the square of the refractive index of the plasma is inversely proportional to the frequency of the wave,

$$n^2 \approx 1 + \frac{\omega_p^2}{\omega_c} \cdot \frac{1}{\omega} \approx \frac{\omega_p^2}{\omega_c} \cdot \frac{1}{\omega}$$

Finally, the phase velocity of the traveling wave can be calculated using the relationship,

$$v_{ph} = \frac{c}{n}$$

where c is the speed of light in a vacuum ($3.0 \times 10^8 m / s$). Considering possible wave frequencies from 0-1000 Hertz, the corresponding phase velocity was calculated and plotted in Figure 24. For frequencies in the ELF/VLF range, the phase velocity of whistler wings appear to be in the 100-1000 kilometer per second range, again far greater than the propagation velocities in the table above.

In conjunction with the PMG radar measurements, the University of Genoa, Italy provided a highly sensitive ground-fixed magnetometer for observations at the Earth's

surface of spontaneous and man-made emissions, propagating from the orbiting tether through the Earth-ionosphere cavity. This super-conducting quantum interference device (SQUID) magnetometer was used to investigate perturbations in the ambient natural magnetic fluctuations during PMG's pass overhead. Although final analysis has not yet been completed, preliminary results so far do not exclude the presence of possible satellite perturbations, such as whistler wings, affecting the ELF background noise. (Minna et al., 1994)

The table below summarizes the various propagational wave calculations made in the preceding paragraphs. Only the oxygen ion thermal velocity appears to be of the same

electron thermal velocity	123 km/sec
O+ ion thermal velocity	0.72 km/sec
Xe+ ion thermal velocity	0.25 km/sec
O+ Alfven velocity	540 km/sec
Xe+ Alfven velocity	189 km/sec
ELF/VLF whistler wave velocity	100-1000 km/sec

order of magnitude as the proposed propagation velocity of the plasma disturbances observed at Hawaii and Jicamarca. This suggests that the traveling disturbances associated with PMG's meridian crossing are ion sound waves, composed of the ambient plasma of the ionosphere. Alternatively, these signals might be thought of as ambipolar diffusion of plasma from the cathodes along the field line at approximately the ion sound speed.(Chen, 1984)

VII. CONCLUSIONS

Multiple observations of the plasma-perturbation signatures associated with PMG meridian crossing supports the concept of disturbances, caused by passage of an electrodynamic tether through the ionospheric plasma, propagating along the magnetic field lines. In each instance, the observed plasma disturbance lasted several seconds and had a propagation velocity of the order of 1000 meters per second. The large distances of propagation suggest that the signals would continue their path along the field lines, until reaching the E layer of the ionosphere. If these signals represent field-aligned currents, this would allow for current loop closure.

The true dynamics of the phantom current loop still remain a mystery, however, further processing of all data collected for each pass during this experiment will provide more detail regarding signal strength, spectral behavior, spatial diffusion, and echo duration. This detail should be more interpretable in terms of field-aligned current flow, current closure phenomenology, and general electrified-spacecraft interactions with the ionospheric environment. The complex sheath structure around a highly charged body moving in a magnetoplasma and the processes occurring there, such as wave generation and plasma expansion phenomena, are still largely unexplored. A large wake is probably characterizing the satellite environment, and wave and particle phenomena associated with this wake, and with the expansion of the outside plasma into this evacuated cavity needs to be investigated.

The concepts for use of tethers in space have been with us for some time. However, the continuing new developments concerning electrodynamic tethers now provide a revolutionary capability for generating propulsion through momentum exchange, and in generating electric power through interactions with the space environment.

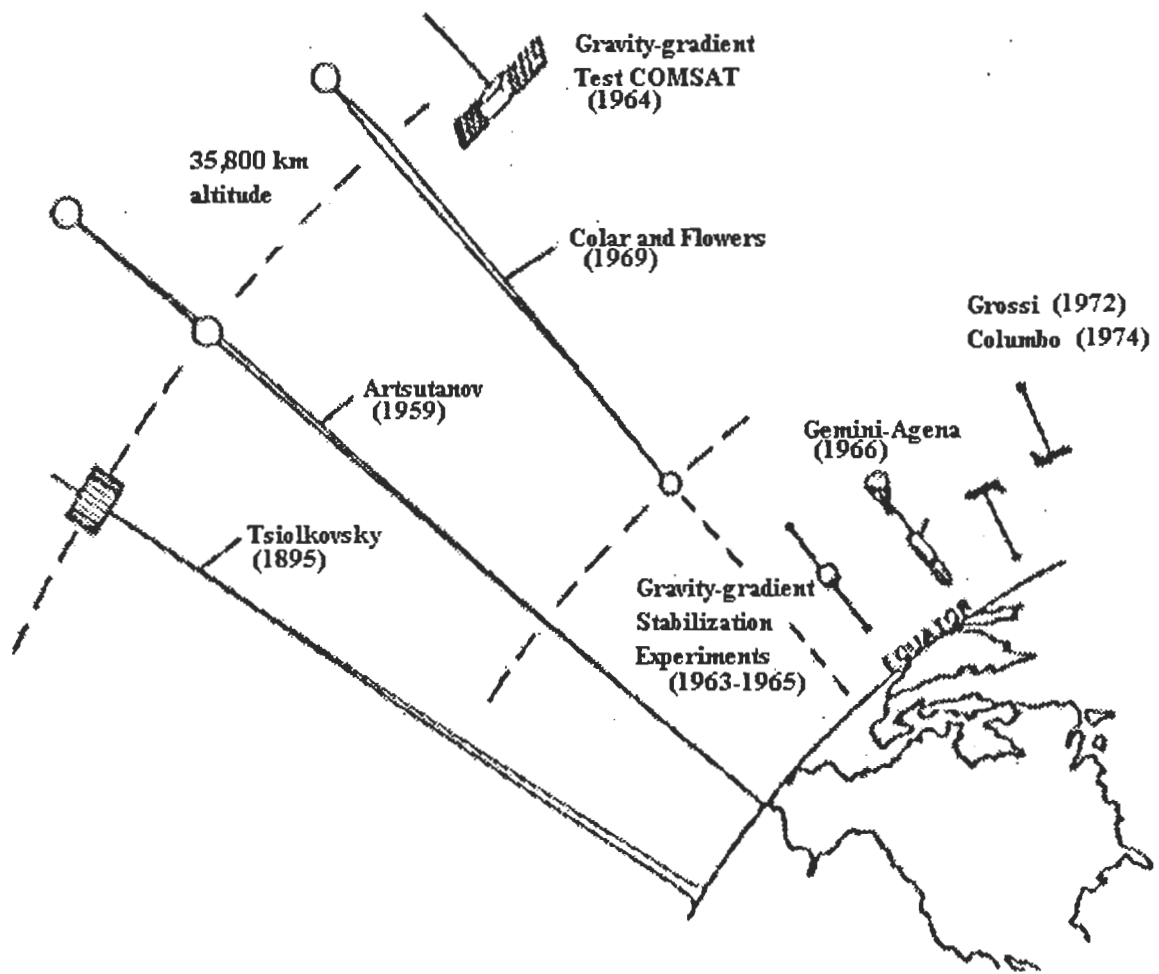


Figure 1: Early Gravity-Gradient Concepts

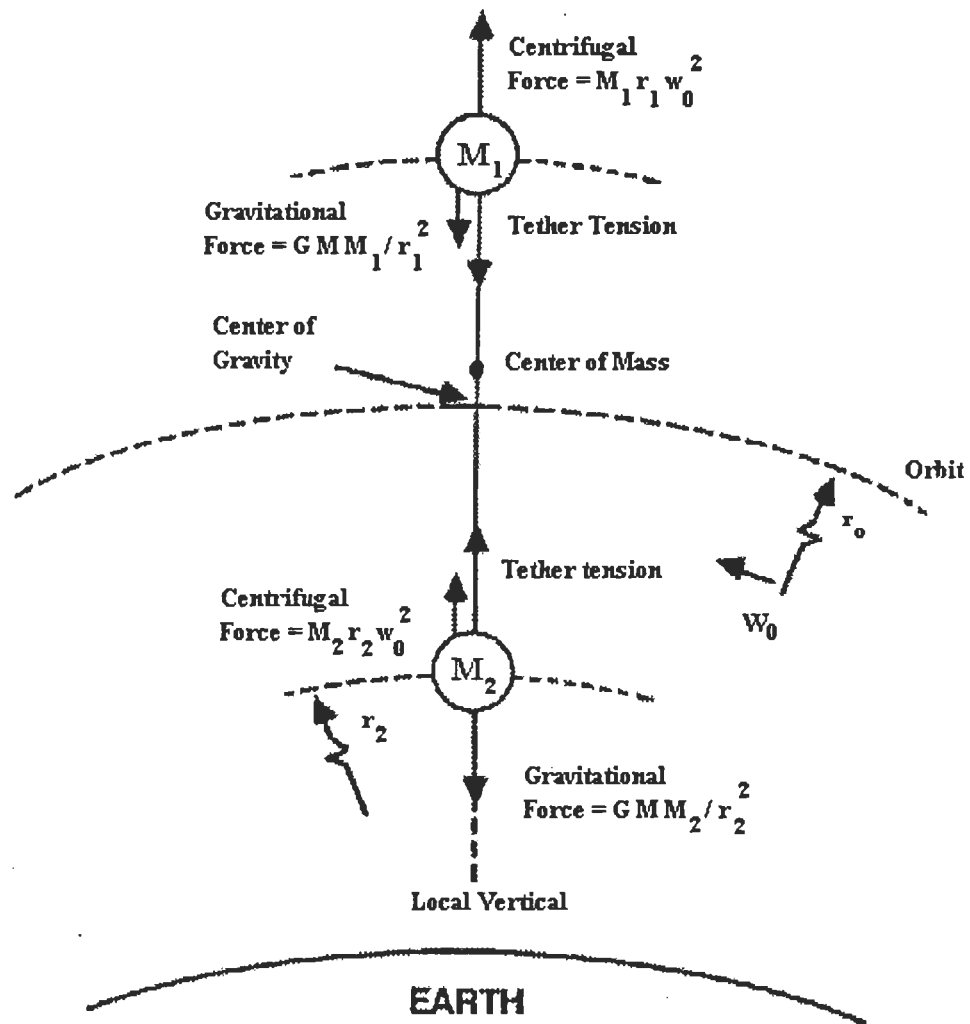


Figure 2: Forces Acting on Tethered Satellites

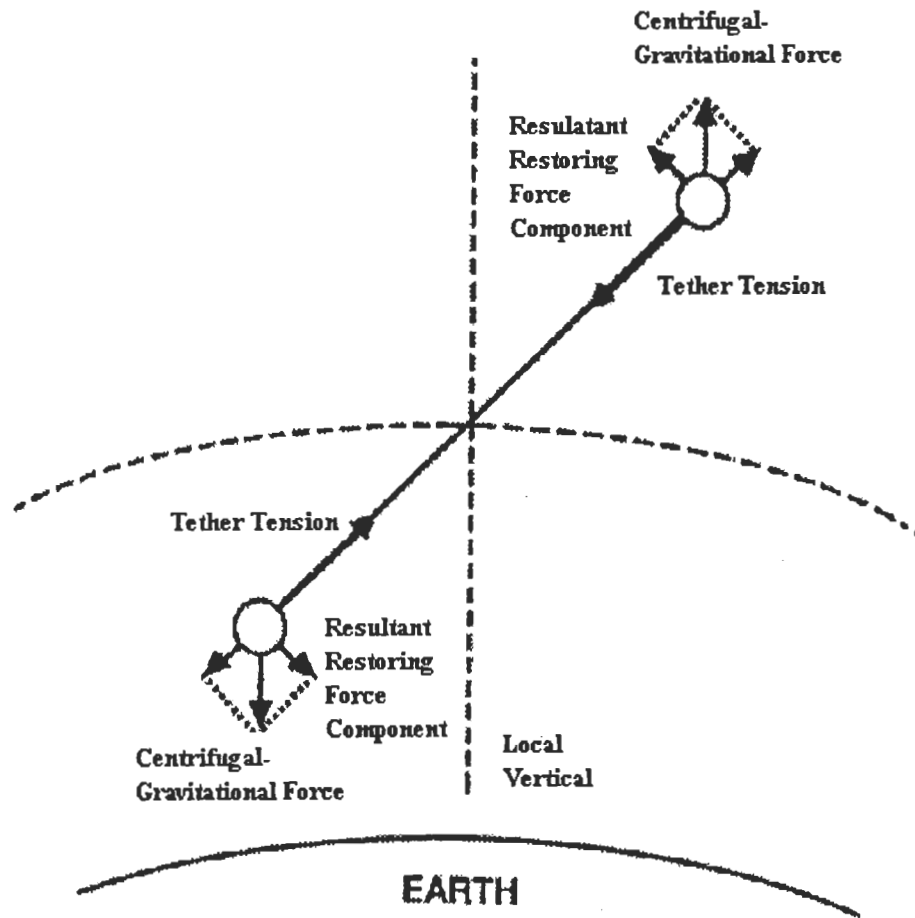


Figure 3: Restoring Forces Acting on Tethered Satellites

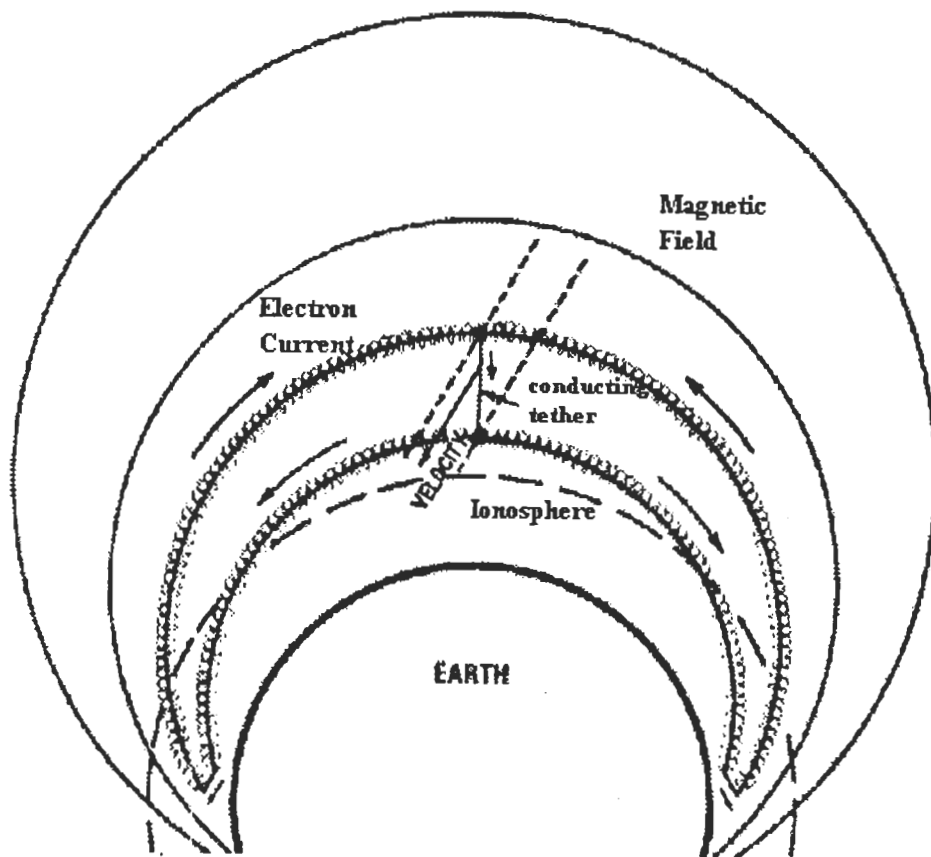


Figure 4: Current Paths for Electrodynamic Tethers

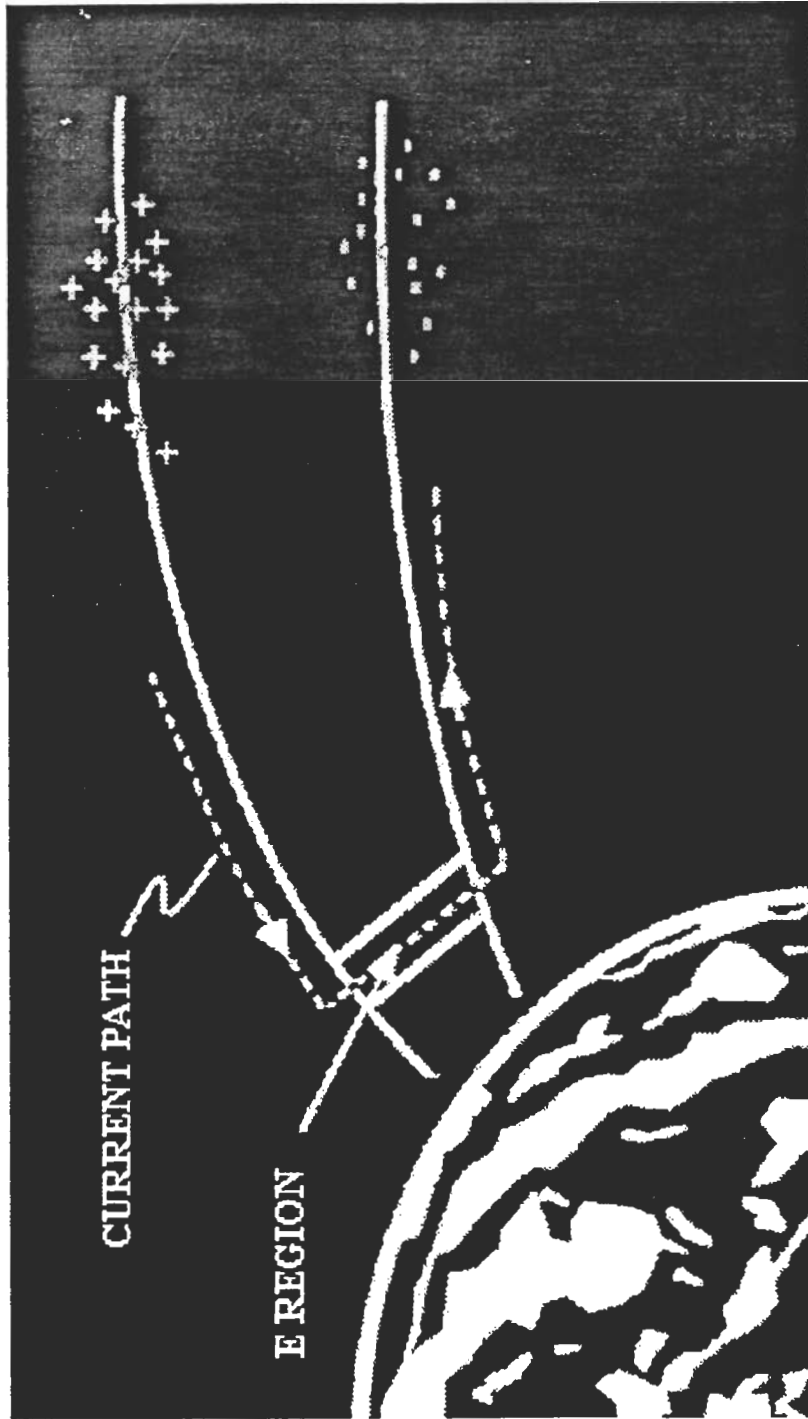


Figure 5: The Phantom Current Loop

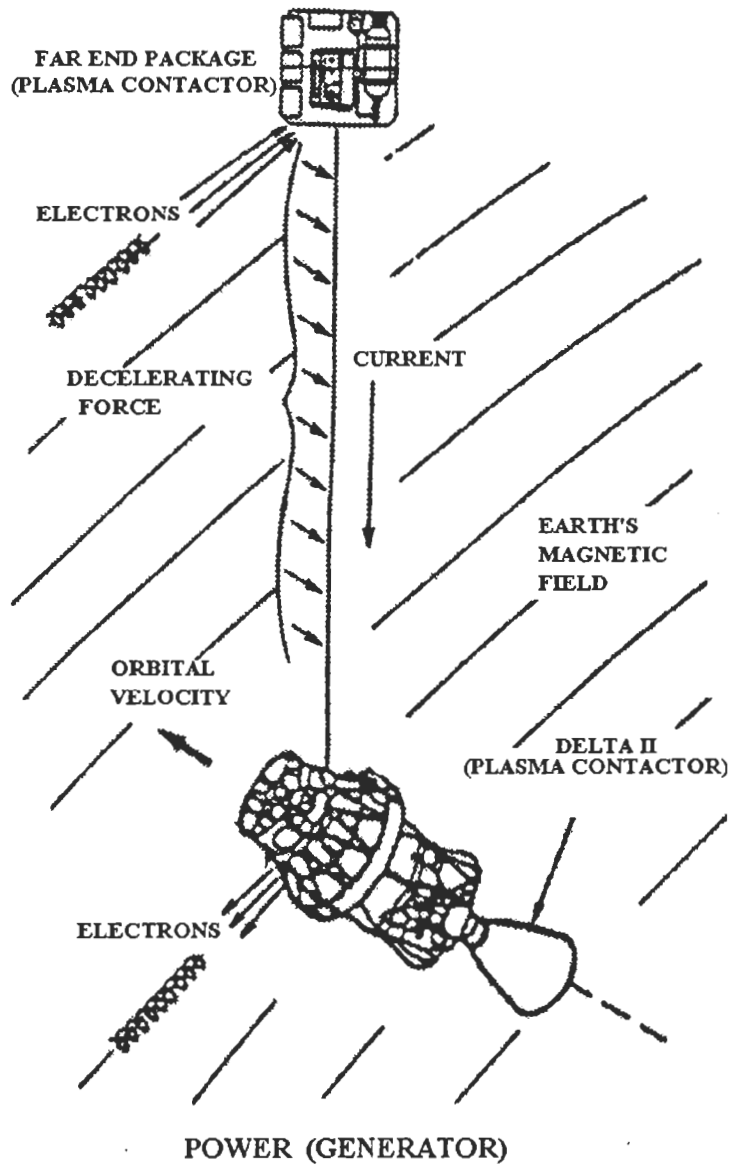


Figure 6: The Generator Principle

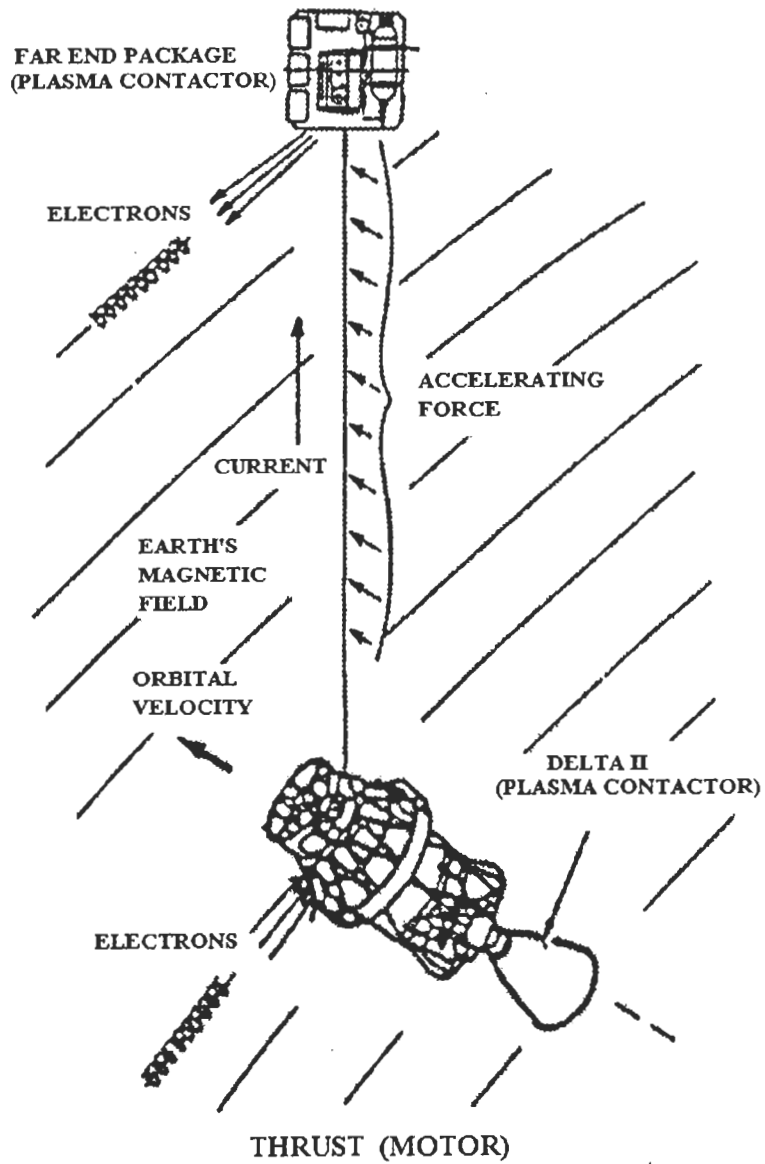


Figure 7: The Motor Principle

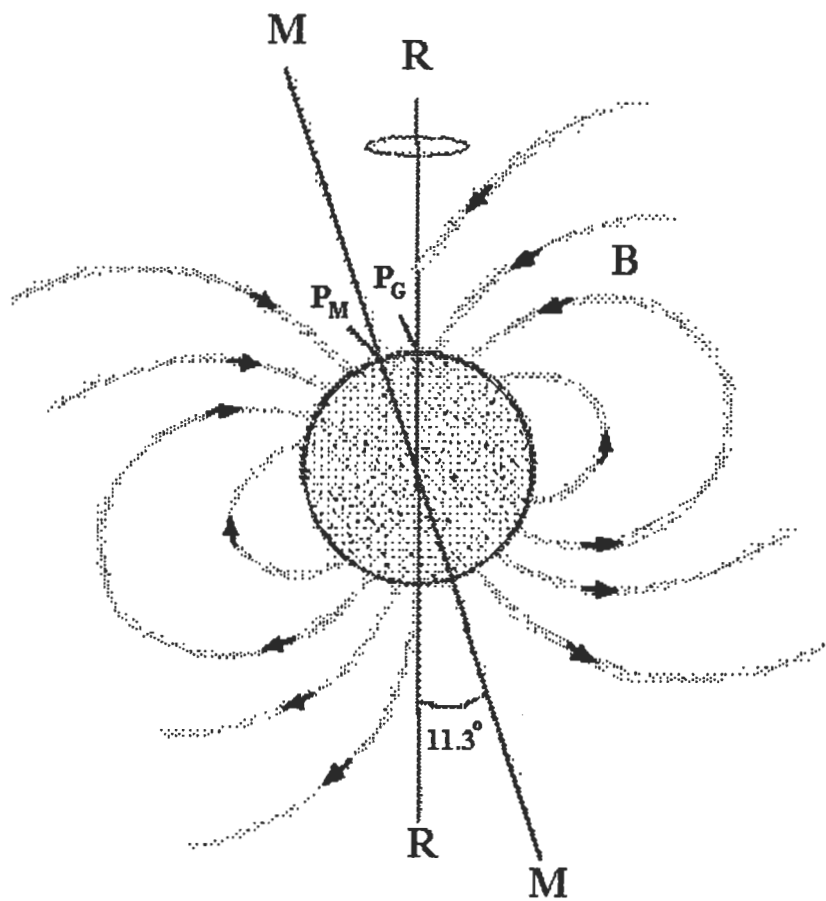


Figure 8: The Eccentric-Dipole Model of the Earth's Magnetic Field

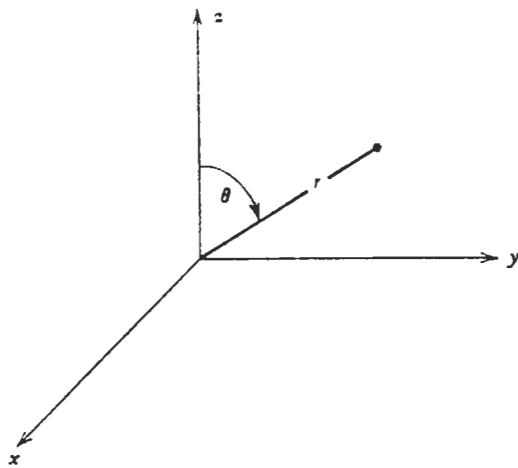


Figure 9: Geometry for a Static Dipole Field

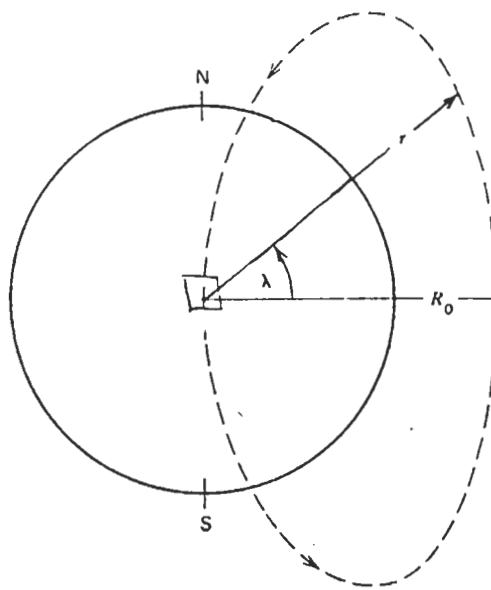


Figure 10: Geomagnetic Latitude and Equatorial Crossing Distance of a Field Line

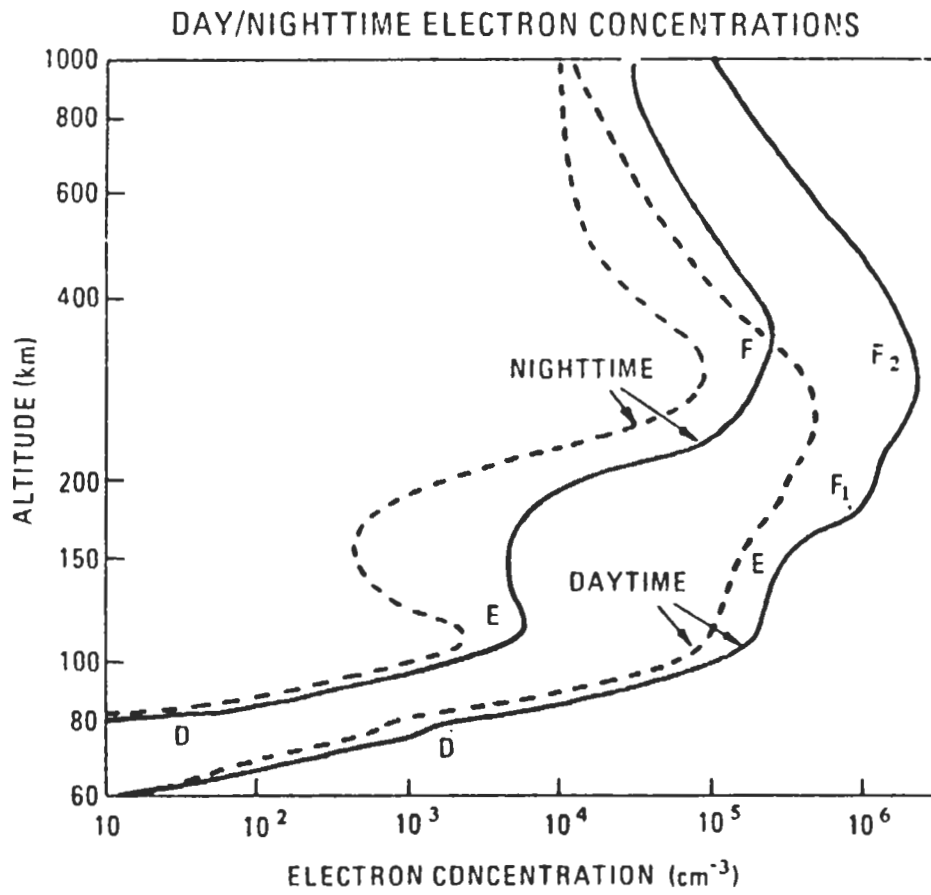


Figure 11: Ionospheric Electron Density Layers

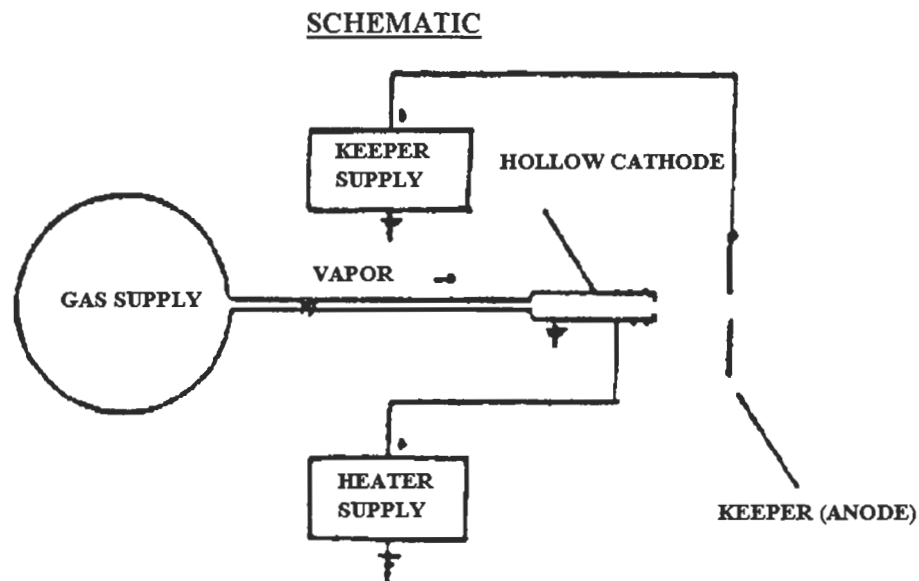
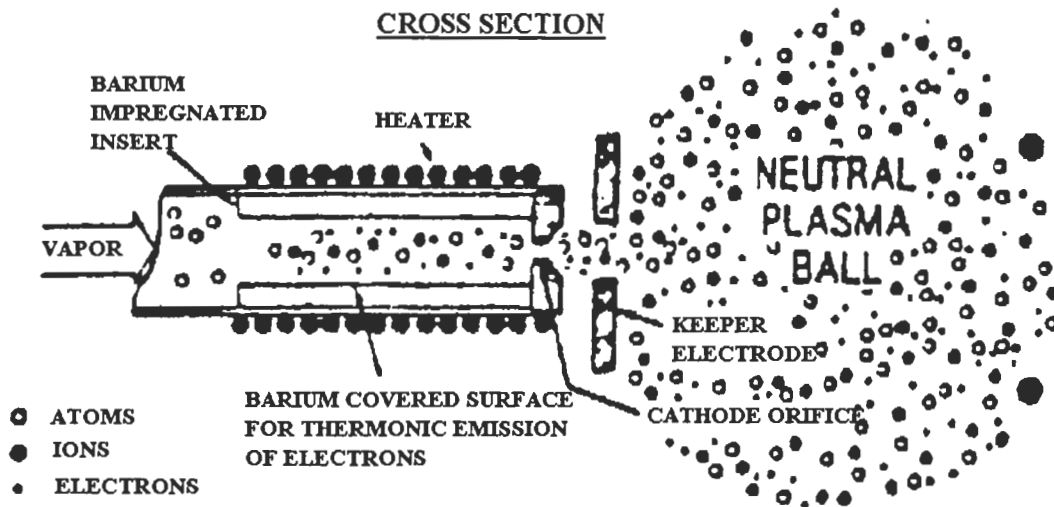


Figure 12: PMG Hollow Cathode Assembly Schematic

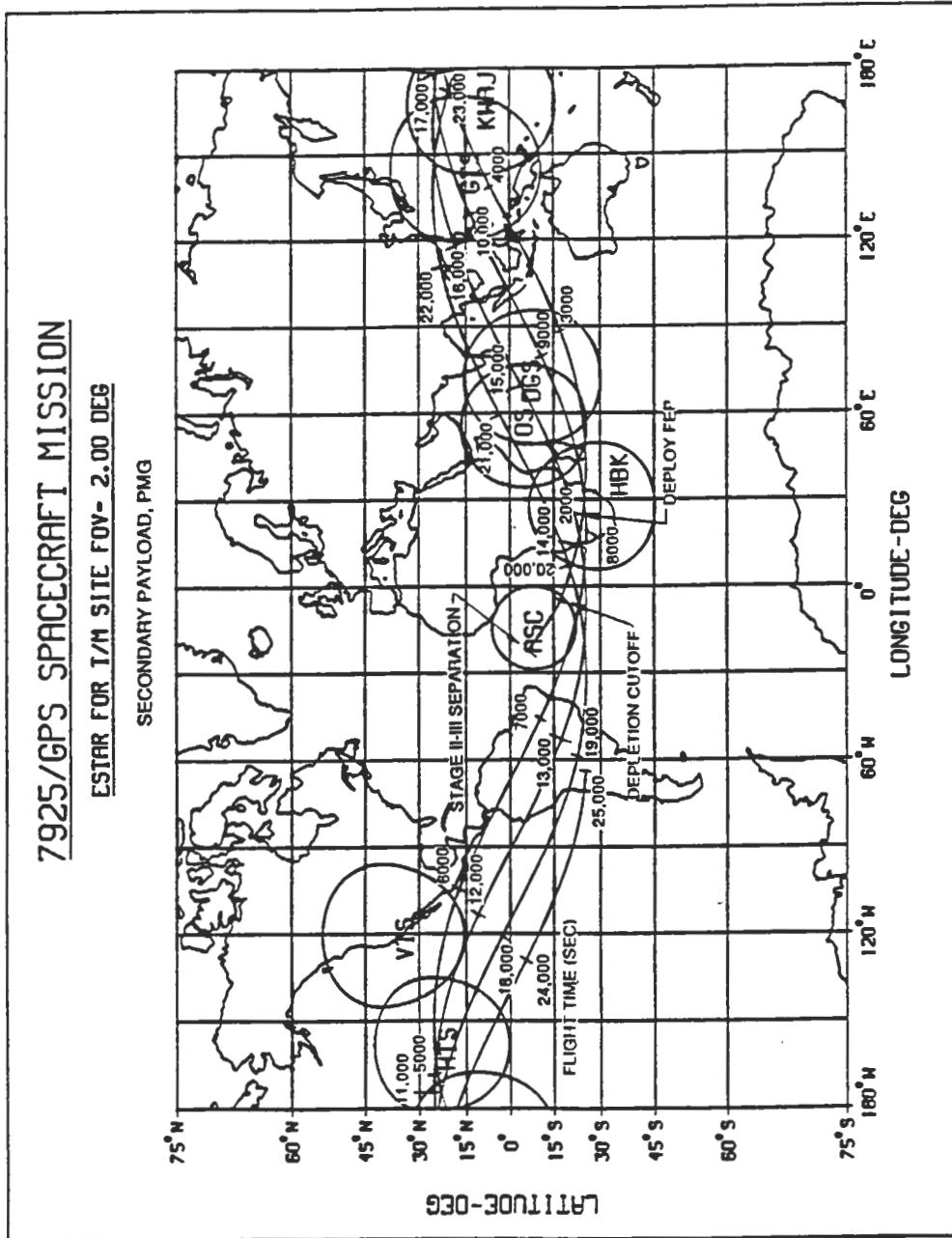


Figure 13: PMG Mission Flight Profile

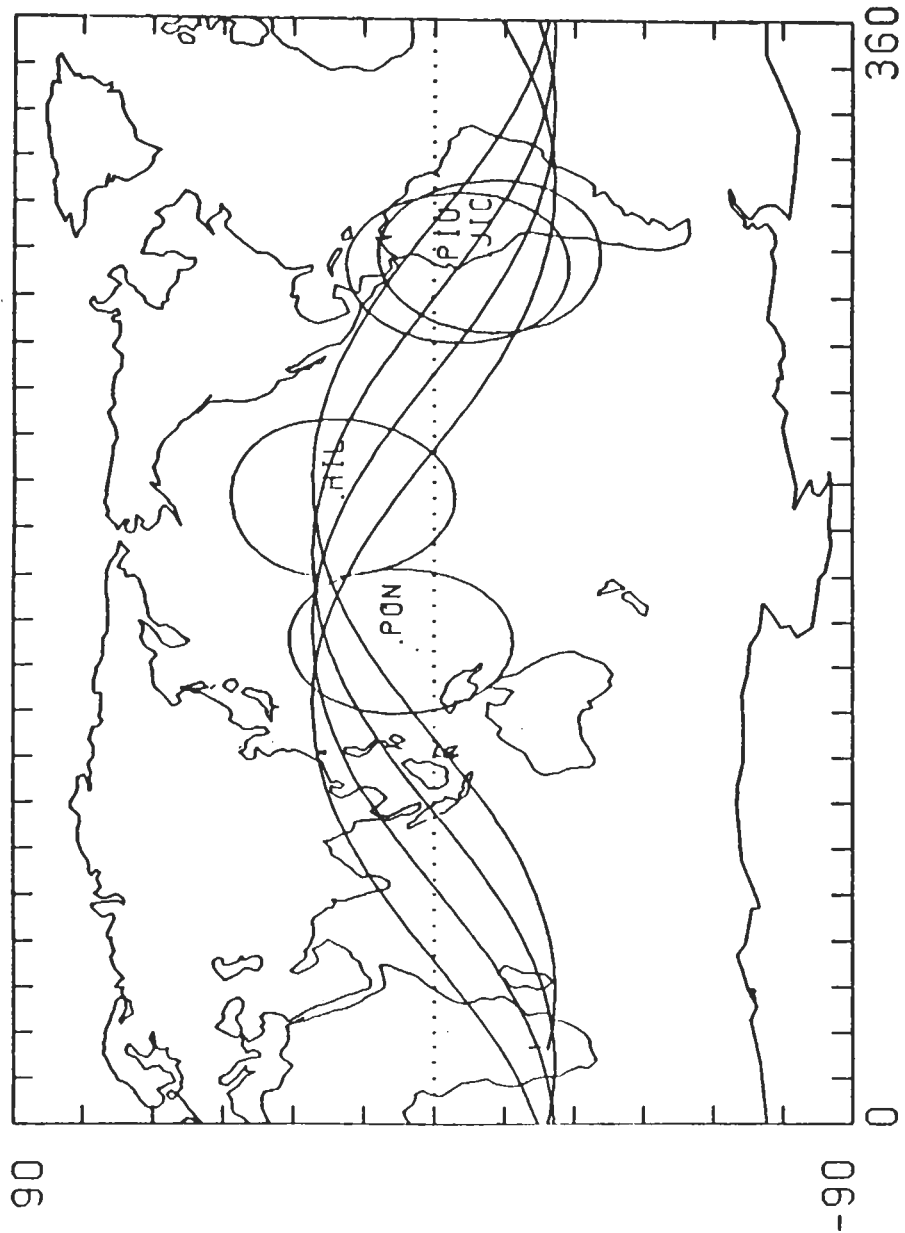


Figure 14: PMG Ground Track and Observing Radar Sites

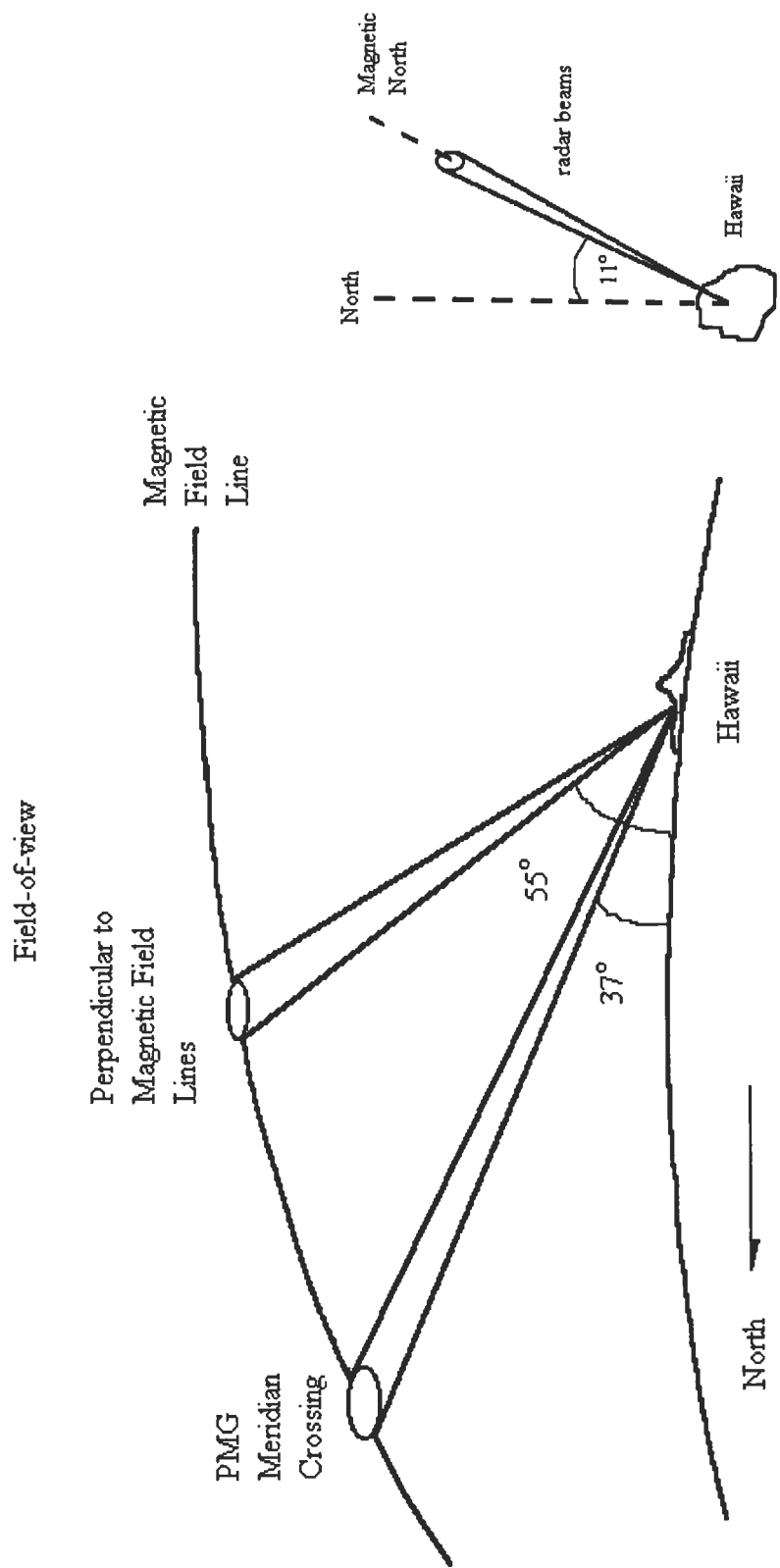


Figure 15: Hawaii Radar Beam Geometry for Pass 1

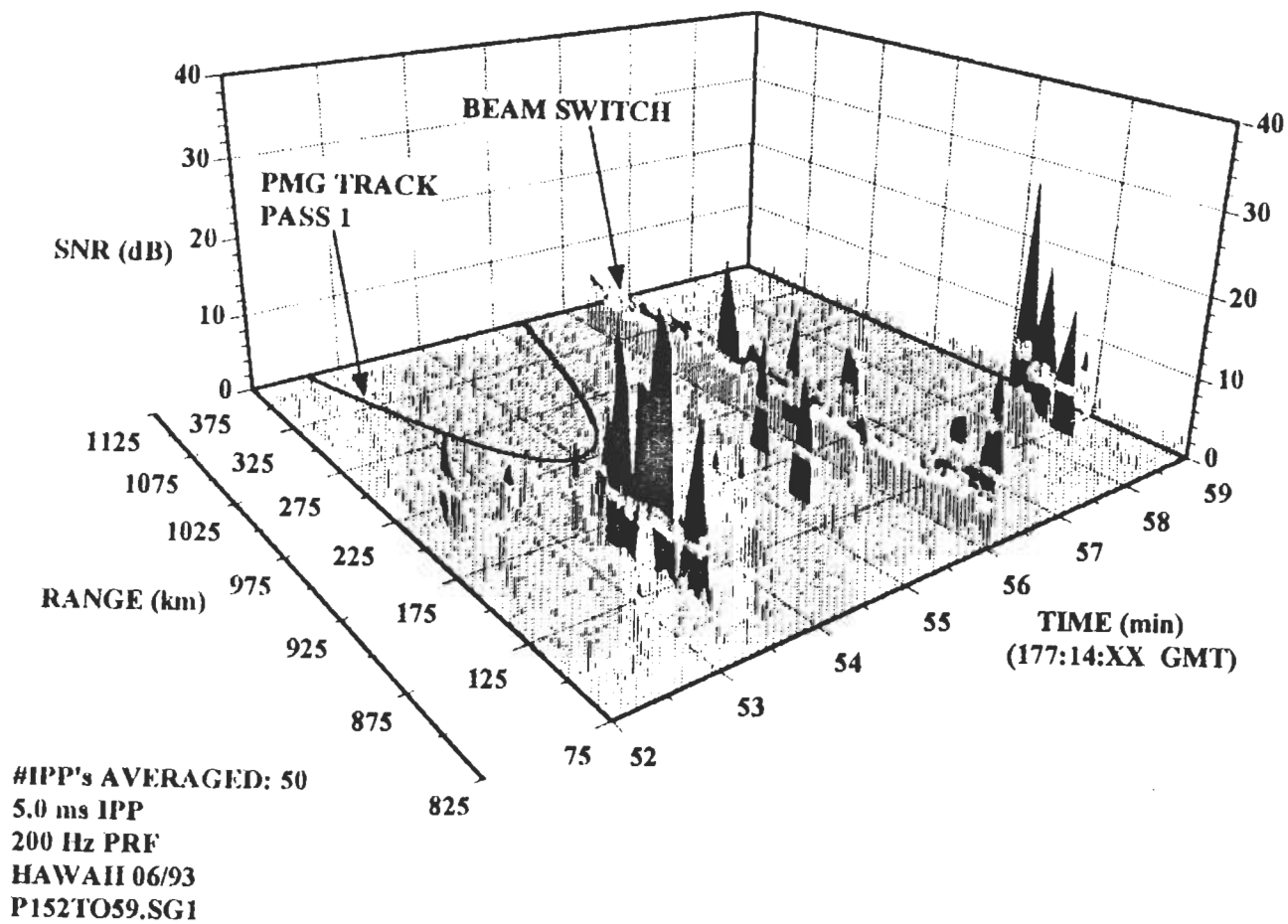


Figure 16: PMG Hawaii Pass 1 Echo Activity (Jost and Stanley, 1994)

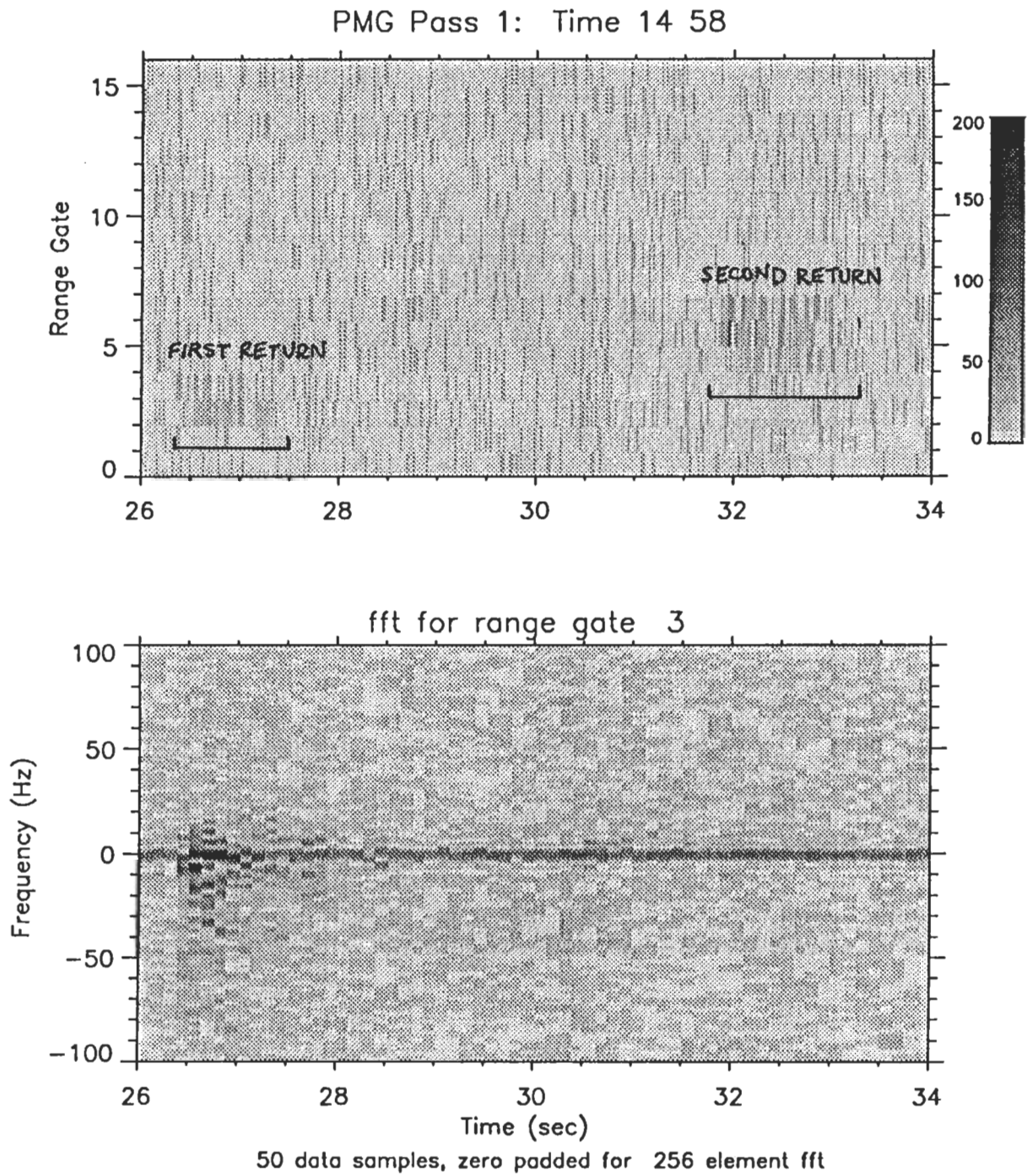


Figure 17: Hawaii Pass 1 Plasma Returns - Range Gate 3

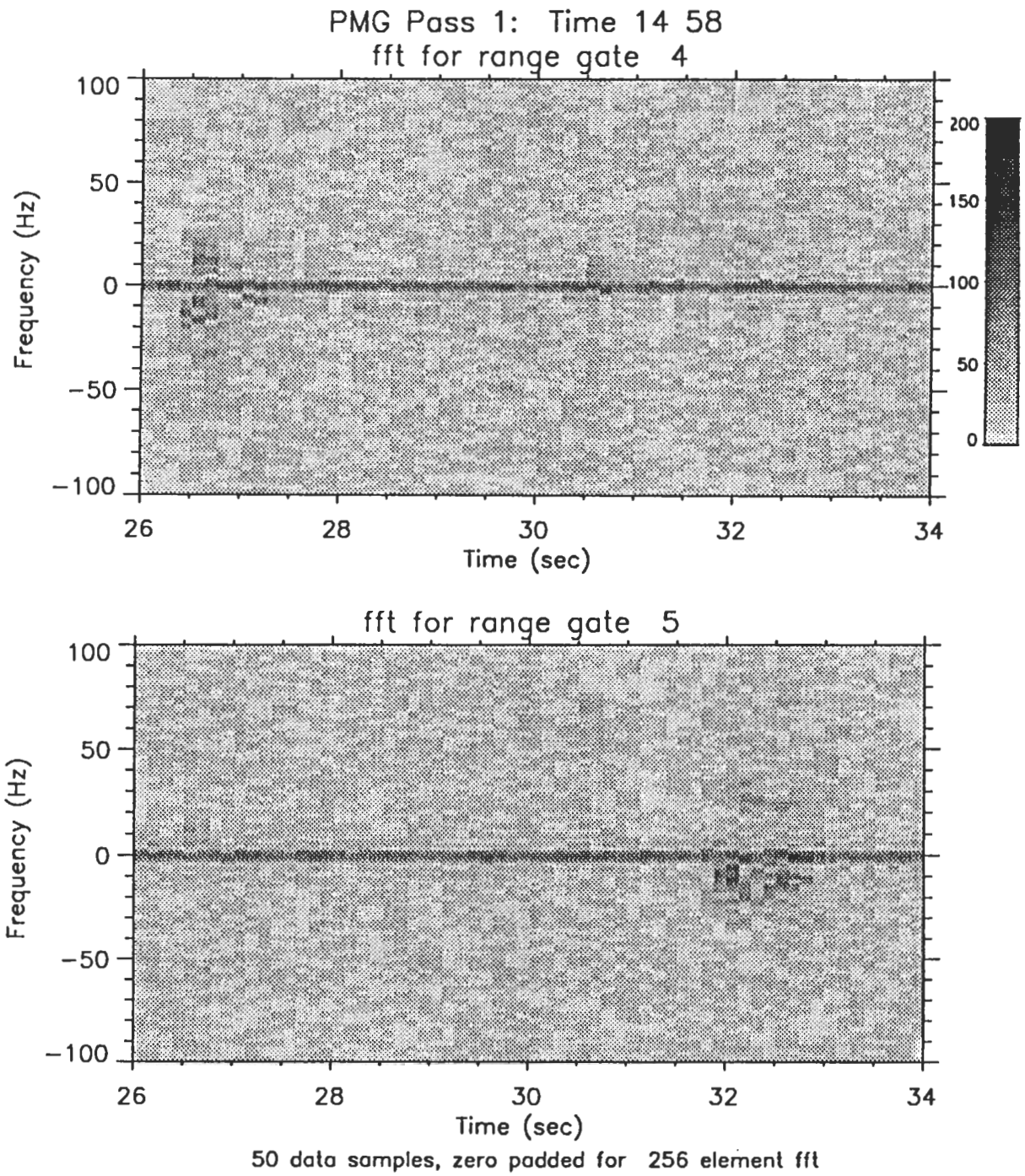


Figure 18: Hawaii Pass 1 Plasma Returns - Range Gates 4 and 5

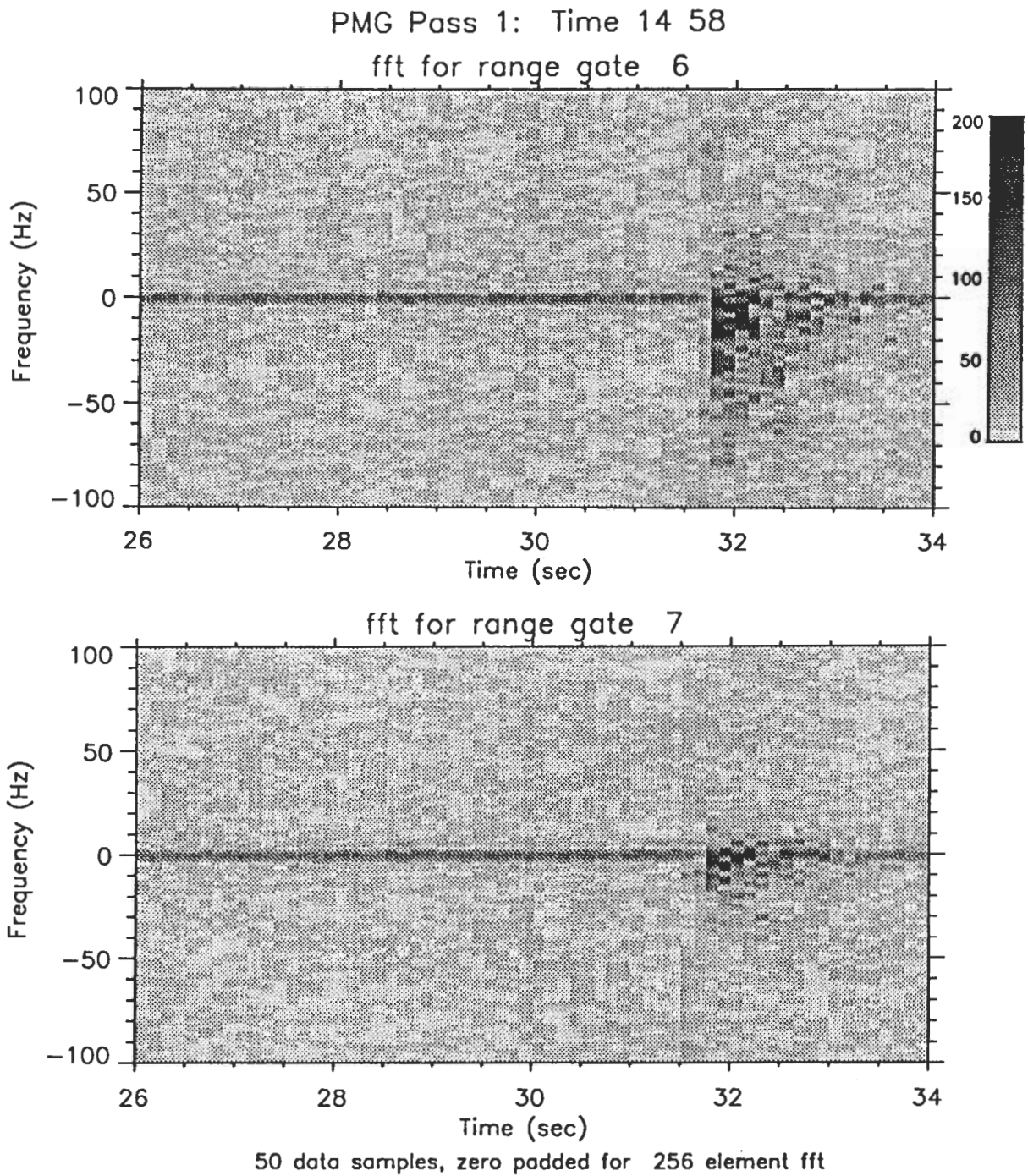


Figure 19: Hawaii Pass 1 Plasma Returns - Range Gates 6 and 7

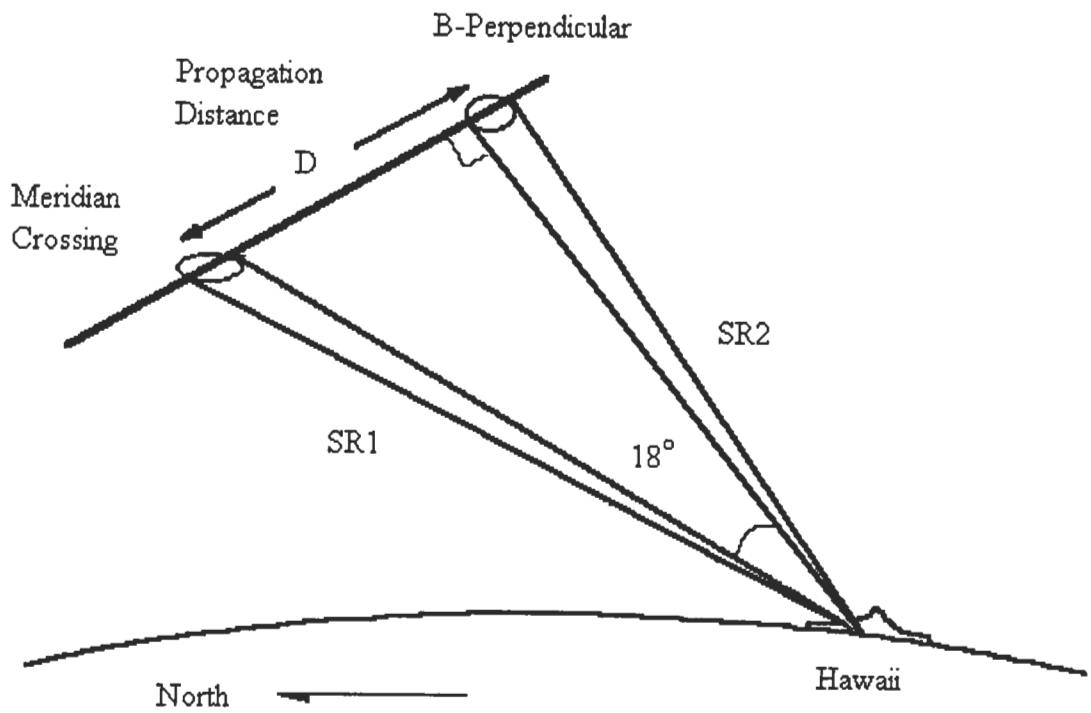


Figure 20: Geometry for Hawaii Pass 1 Calculations

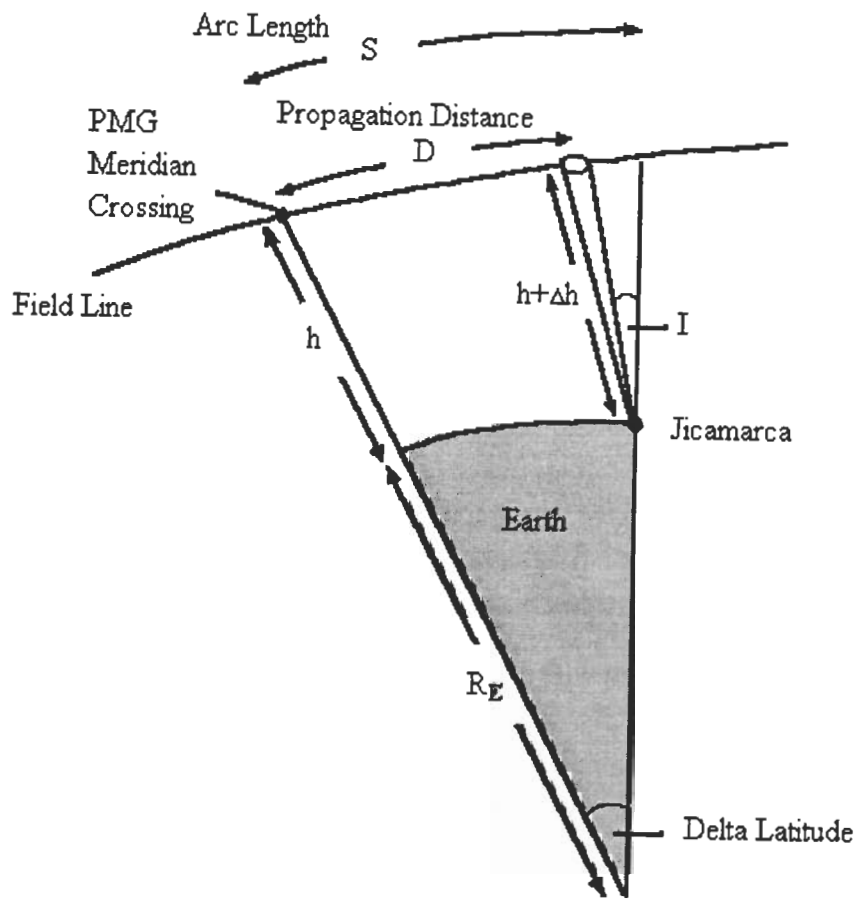


Figure 21: Geometry for Jicamarca Pass 2 Calculations

**FLUX-TUBE MAPPING OVER JICAMARCA
AT GEOMAGNETIC MERIDIAN**

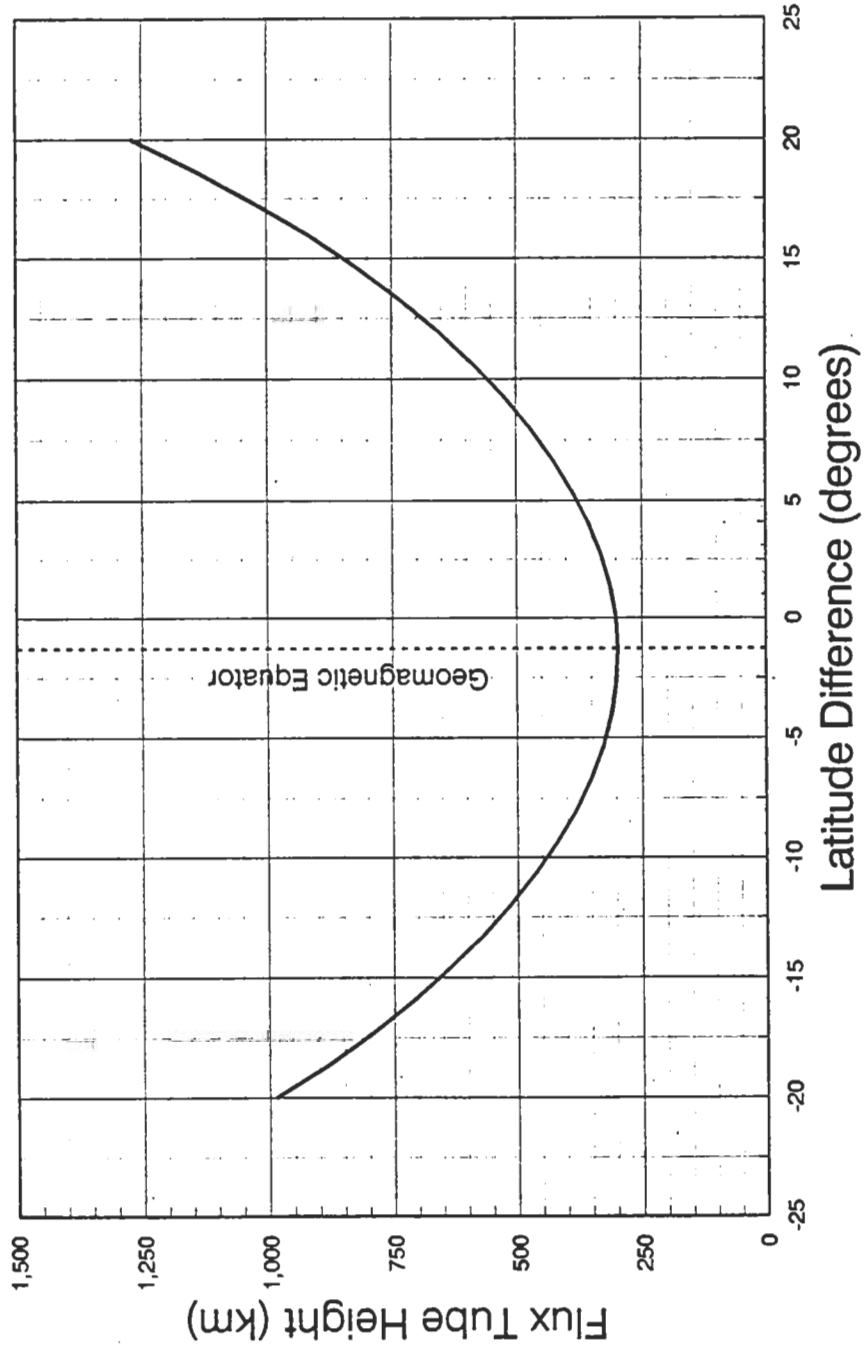


Figure 22: Flux-Tube Height Variations Relative to Jicamarca

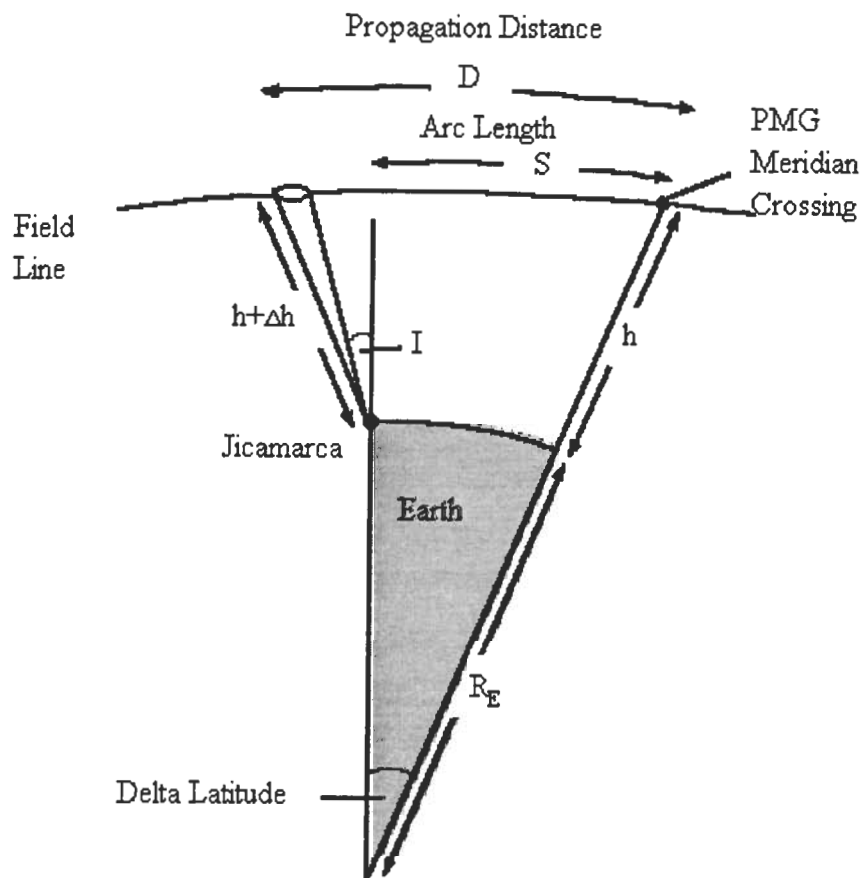


Figure 23: Geometry for Jicamarca Pass 3 and 4 Calculations

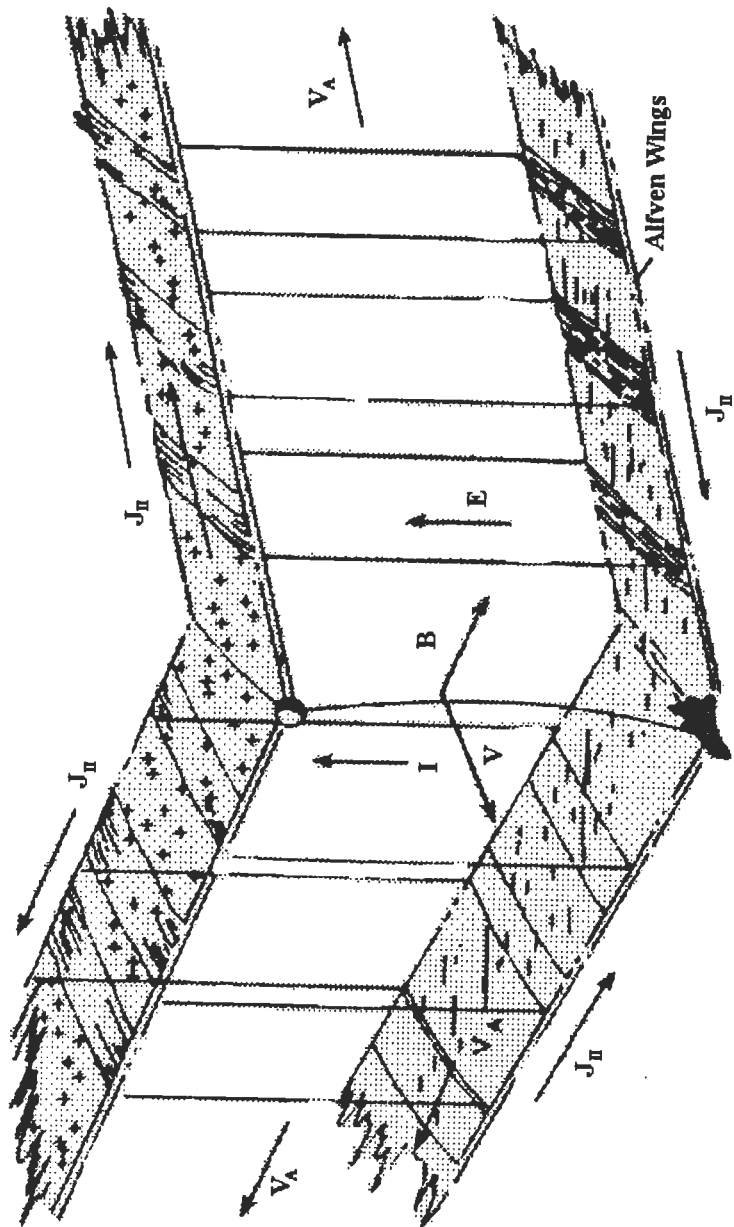


Figure 24: Formation of Alfvén Wings

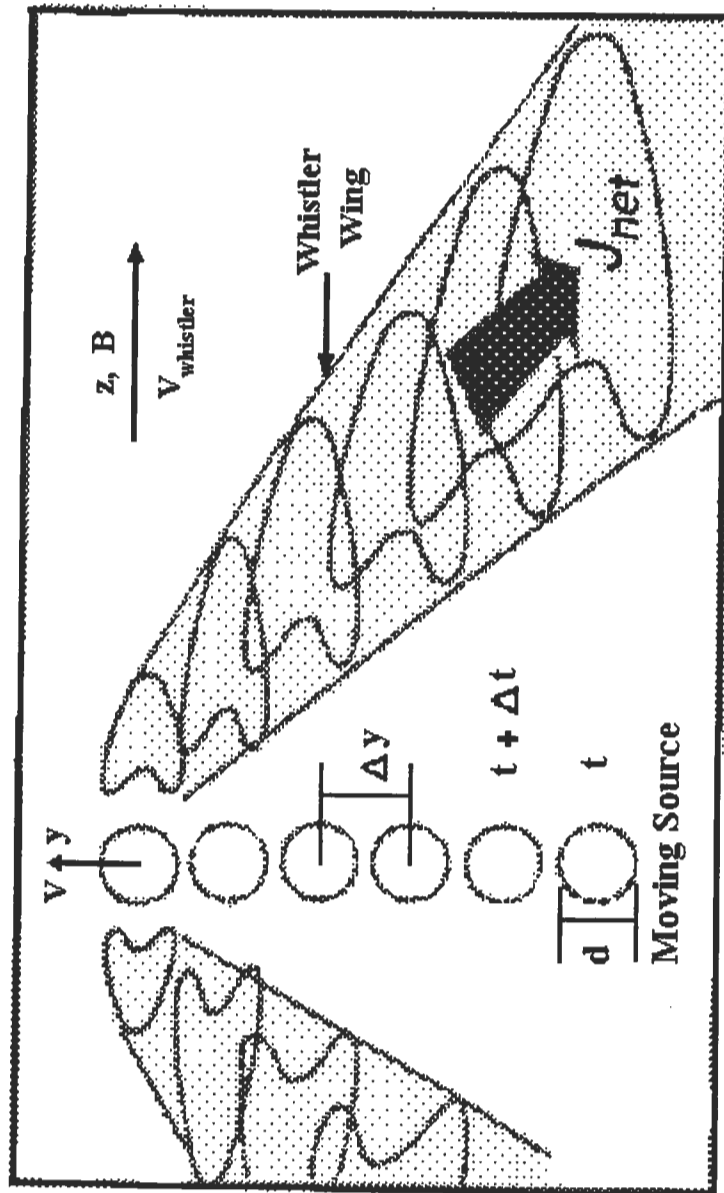


Figure 25: Formation of Whistler Wings

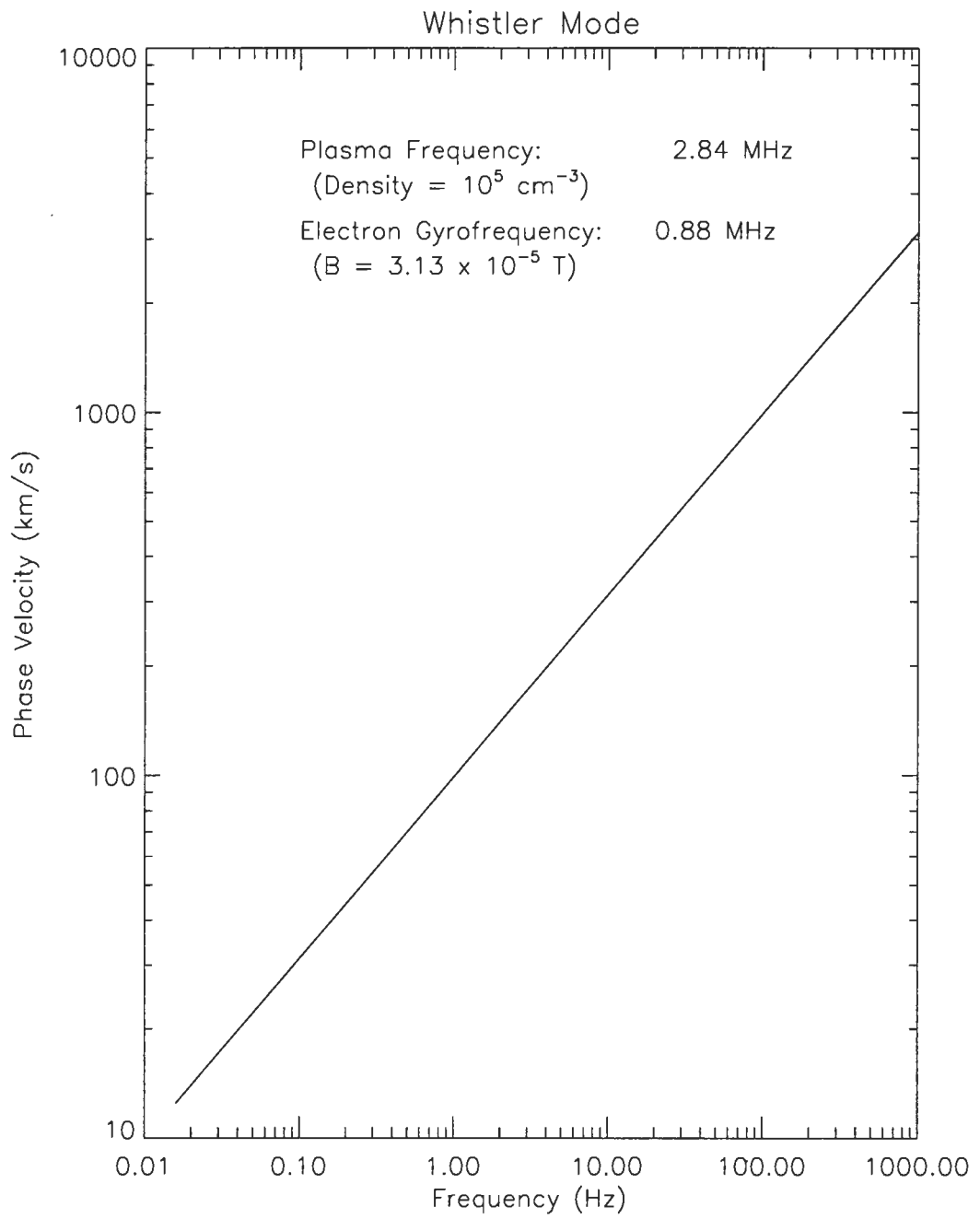


Figure 26: Whistler Mode Phase Velocity/Frequency Relationship

TABLE 1: PMG MERIDIAN CROSSING FOR HAWAII PASS 1

Time YYDDHHMMSS.SSS	PMG Position			RADAR Look Angles		
	North Lat DEG	East Long DEG	Height KM	Elevation DEG	Azimuth DEG	Range KM
93177145410.000	25.7811	205.9492	644.360	38.0825	6.5878	976.020
93177145411.020	25.7829	206.0139	644.010	38.0233	7.1039	976.560
93177145412.040	25.7847	206.0786	643.659	37.9617	7.6186	977.144
93177145413.060	25.7864	206.1433	643.307	37.8976	8.1317	977.773
93177145414.080	25.7882	206.2081	642.956	37.8311	8.6433	978.447
93177145415.100	25.7899	206.2728	642.605	37.7622	9.1532	979.165
93177145416.120	25.7915	206.3376	642.253	37.6910	9.6613	979.928
93177145417.140	25.7932	206.4024	641.901	37.6174	10.1677	980.735
93177145418.160	25.7948	206.4672	641.549	37.5415	10.6722	981.587
93177145419.180	25.7963	206.5320	641.197	37.4633	11.1748	982.483
93177145420.200	25.7979	206.5968	640.845	37.3829	11.6754	983.422
93177145421.220	25.7994	206.6616	640.492	37.3002	12.1740	984.406
93177145422.240	25.8008	206.7264	640.140	37.2153	12.6704	985.433
93177145423.260	25.8023	206.7912	639.787	37.1283	13.1647	986.505
93177145424.280	25.8037	206.8560	639.434	37.0391	13.6568	987.619
93177145425.300	25.8050	206.9209	639.081	36.9479	14.1465	988.777
93177145426.320	25.8064	206.9857	638.728	36.8546	14.6339	989.979
93177145427.340	25.8077	207.0506	638.374	36.7592	15.1190	991.223
93177145428.360	25.8090	207.1155	638.021	36.6619	15.6015	992.511
93177145429.380	25.8102	207.1803	637.667	36.5626	16.0816	993.841

TABLE 2: PMG MERIDIAN CROSSING FOR JICAMARCA PASS 2

Time YYDDHHMMSS.SSS	PMG Position			RADAR Look Angles		
	North Lat DEG	East Long DEG	Height KM	Elevation DEG	Azimuth DEG	Range KM
93177165652.440	-6.9275	283.0247	193.386	16.3618	358.8210	595.745
93177165653.460	-6.9576	283.0853	193.367	16.4841	359.5099	592.463
93177165654.480	-6.9875	283.1459	193.349	16.6046	0.2072	589.260
93177165655.500	-7.0175	283.2066	193.331	16.7233	0.9130	586.139
93177165656.520	-7.0475	283.2672	193.314	16.8401	1.6270	583.099
93177165657.540	-7.0775	283.3279	193.297	16.9547	2.3494	580.142
93177165658.560	-7.1074	283.3885	193.281	17.0672	3.0799	577.270
93177165659.580	-7.1374	283.4492	193.265	17.1772	3.8185	574.484
93177165700.600	-7.1673	283.5098	193.250	17.2849	4.5651	571.785
93177165701.620	-7.1972	283.5705	193.235	17.3899	5.3195	569.174
93177165702.640	-7.2272	283.6312	193.221	17.4921	6.0816	566.652
93177165703.660	-7.2571	283.6919	193.207	17.5916	6.8513	564.222
93177165704.680	-7.2870	283.7526	193.194	17.6880	7.6284	561.883
93177165705.700	-7.3169	283.8133	193.181	17.7813	8.4126	559.638
93177165706.720	-7.3468	283.8741	193.168	17.8714	9.2039	557.487
93177165707.740	-7.3767	283.9348	193.156	17.9581	10.0019	555.431
93177165708.760	-7.4065	283.9955	193.145	18.0413	10.8065	553.471
93177165709.780	-7.4364	284.0563	193.134	18.1209	11.6175	551.609
93177165710.800	-7.4663	284.1171	193.123	18.1967	12.4345	549.845
93177165711.820	-7.4961	284.1778	193.113	18.2687	13.2573	548.181
93177165712.840	-7.5259	284.2386	193.103	18.3368	14.0857	546.617

TABLE 3: PMG MERIDIAN CROSSING FOR JICAMARCA PASS 3

Time YYDDHHMMSS.SSS	PMG Position			RADAR Look Angles		
	North Lat DEG	East Long DEG	Height KM	Elevation DEG	Azimuth DEG	Range KM
93177183818.360	-17.0816	281.8900	213.622	17.1099	193.0675	630.151
93177183819.380	-17.1054	281.9552	213.755	17.0852	192.3453	631.158
93177183820.400	-17.1291	282.0204	213.888	17.0574	191.6257	632.253
93177183821.420	-17.1528	282.0856	214.022	17.0264	190.9089	633.436
93177183822.440	-17.1765	282.1508	214.157	16.9924	190.1951	634.705
93177183823.460	-17.2002	282.2161	214.292	16.9554	189.4846	636.061
93177183824.480	-17.2238	282.2813	214.427	16.9153	188.7774	637.503
93177183825.500	-17.2474	282.3466	214.563	16.8724	188.0738	639.030
93177183826.520	-17.2710	282.4119	214.699	16.8266	187.3740	640.642
93177183827.540	-17.2946	282.4772	214.835	16.7779	186.6782	642.337
93177183828.560	-17.3181	282.5425	214.972	16.7266	185.9864	644.116
93177183829.580	-17.3416	282.6079	215.110	16.6725	185.2990	645.978
93177183830.600	-17.3651	282.6732	215.247	16.6159	184.6159	647.921
93177183831.620	-17.3886	282.7386	215.386	16.5567	183.9475	649.946
93177183832.640	-17.4120	282.8039	215.524	16.4950	183.2637	652.051
93177183833.660	-17.4354	282.8693	215.663	16.4309	182.5948	654.236
93177183834.680	-17.4588	282.9347	215.803	16.3645	181.9309	656.499
93177183835.700	-17.4822	283.0002	215.943	16.2958	181.2720	658.841
93177183836.720	-17.5055	283.0656	216.083	16.2249	180.6184	661.259
93177183837.740	-17.5288	283.1310	216.224	16.1519	179.9700	663.754
93177183838.760	-17.5521	283.1965	216.365	16.0768	179.3271	666.325

TABLE 4: PMG MERIDIAN CROSSING FOR JICAMARCA PASS 4

Time YYDDHHMMSS.SSS	PMG Position			RADAR Look Angles		
	North Lat DEG	East Long DEG	Height KM	Elevation DEG	Azimuth DEG	Range KM
93177201900.600	-23.5893	281.1635	280.265	5.9033	189.0860	1360.237
93177201901.620	-23.6023	281.2332	280.521	5.9101	188.7714	1360.551
93177201902.640	-23.6153	281.3030	280.778	5.9165	188.4569	1360.903
93177201903.660	-23.6282	281.3728	281.036	5.9223	188.1427	1361.292
93177201904.680	-23.6411	281.4425	281.293	5.9277	187.8286	1361.720
93177201905.700	-23.6540	281.5123	281.551	5.9325	187.5147	1362.185
93177201906.720	-23.6668	281.5821	281.809	5.9369	187.2010	1362.687
93177201907.740	-23.6796	281.6519	282.068	5.9408	186.8875	1363.227
93177201908.760	-23.6923	281.7217	282.327	5.9441	186.5744	1363.805
93177201909.780	-23.7050	281.7915	282.586	5.9470	186.2614	1364.419
93177201910.800	-23.7177	281.8614	282.845	5.9494	185.9488	1365.072
93177201911.820	-23.7304	281.9312	283.105	5.9513	185.6365	1365.761
93177201912.840	-23.7430	282.0010	283.365	5.9527	185.3245	1366.488
93177201913.860	-23.7555	282.0709	283.626	5.9536	185.0128	1367.252
93177201914.880	-23.7681	282.1408	283.886	5.9540	184.7015	1368.054
93177201915.900	-23.7806	282.2106	284.147	5.9539	184.3906	1368.892
93177201916.920	-23.7930	282.2805	284.408	5.9534	184.0800	1369.767
93177201917.940	-23.8054	282.3504	284.670	5.9524	183.7699	1370.679
93177201918.960	-23.8178	282.4203	284.932	5.9508	183.4601	1371.628
93177201919.980	-23.8302	282.4902	285.194	5.9488	183.1509	1372.614

LIST OF REFERENCES

Arnold, David A., *Tether Tutorial*, Conference Proceedings on Space Tethers for Science in the Space Station Era, Venice, 4-8 October 1987.

Artsutanov, Yu, 1960, *V kosmos na elektrovoze*, Kosmosomolskaya Pravda, 31 July.

Bainum, P.M., Ivan Bekey, Luciano Guerriero, and P.A. Penzo, Tethers in Space, *Advances in the Astronautical sciences, Volume 62*, Conference Proceedings, Arlington, VA., September 17-19, 1986.

Brewster, Wayne, *Space Tether - Radar Data Processing*, Masters Thesis, Naval Postgraduate School, September 1994.

Chen, Francis F., *Introduction to Plasma Physics and Controlled Fusion, Volume 1: Plasma Physics*, 1984.

Collar, A.R. and J.W. Flower, 1969, A (relatively) Low Altitude 24-Hour Satellite, *Journal of the British Interplanetary Society*, 22, pp. 442-457.

Colombo, G., Gaposchkin, E.M., Grossi, M.D., and Weiffenbach, G.C., *Shuttle-borne Skyhook: A New Tool for Low Orbital Attitude Research*, Smithsonian Astrophysical Observatory Report, 1974.

Dobrowolny, M. and E. Melchioni, Electrodynamic Aspects of the First Tethered Satellite Mission, *Journal of Geophysical Research, Vol. 98, No. A8*, pages 13,761-13,778, August 1, 1993.

Grossi, M.D., *A UHF Dipole Antenna on a Spaceborne Platform of the PPEL Class*, Letter Report to NASA-MSFC, Contract NAS8-28303, May 11, 1973.

Heinz, Otto and R.C. Olsen, *Introduction to the Space Environment*, PH2514 Text, June 1993.

Jost, R.J. and J.F. Stanley, *Plasma Motor Generator (PMG) Mission Report: Ground-Based Ionospheric Sensor Observations*, February 1994.

Lang, D.L. and R.K. Nolting, *Operation With Tethered Space Vehicles, Gemini Summary Conference*, Manned Spacecraft Center, NASA SP-138, 1967.

Lilley Jr., J.R., A. Greb, I. Katz, A. Davis, J.E. McCoy, J Galofare, and D.C. Ferguson, *Comparison of Theoretical Calculations with Plasma Motor Generator (PMG) Experimental Data*, AIAA Paper #94-0328, 2nd Aerospace Sciences Meeting & Exhibit, Reno, NV., January 10-13, 1994.

Liu, C.H., and Belva Edwards, *Middle Atmosphere Program*, Handbook for MAP, Volume 28, August 1989.

Minna, L., C. Ottonello, S. Pagnan, and G. Tacconi, *Emissions from Orbiting Tethered Satellite Systems to the Earth's Surface: Data Analysis*, IGARSS Conference, Pasadena, August 8-12, 1994.

Moore, R.D., 1966, *The Geomagnetic Thruster - A High Performance Alfvén-Wave Propulsion System Utilizing Plasma Contacts*, AIAA Paper #66-257.

NASA Report, May 1989, *Tether Fundamentals, Tethers in Space Handbook - Second Edition*, pp. 101-136.

NASA Report, 1993, *The First Mission of the Tethered Satellite System (TSS-1)*.

Olsen, R.C., Modification of Spacecraft Potentials by Plasma Emission, *Journal of Spacecraft and Rockets*, Volume 18, Number 5, Sep-Oct 1981, p. 462.

Tascione, Thomas F., *Introduction to the Space Environment*, pp. 33-37, 1988.

Tsiolkovsky, K.E., 1895, *Grezi o zemie i nebe (Dreams of Earth and Sky)*, Moscow, Isd-vo AN-SSSR, p. 35.

Urrutia, J.M., R.L. Stenzel and C.L. Rousculp, Three-dimensional Currents of Electrodynamic Tethers Obtained from Laboratory Models, *Geophysical Research Letters*, Vol. 21, No. 6, March 15, 1994.

INITIAL DISTRIBUTION LIST

1. Defense Technical Information Center 2
Cameron Station
Alexandria, VA. 22304-6145
2. Library, Code 52 2
Naval Postgraduate School
Monterey, CA. 93943-5101
3. Department Chairman, Code SP 1
Space Systems Academic Group
Naval Postgraduate School
Monterey, CA. 93943-5002
4. Dr. R.C. Olsen, Code Ph/OS 5
Department of Physics
Naval Postgraduate School
Monterey, CA. 93943-5002
5. Dr. S. Gnanalingam, Code Ph/GM 1
Department of Physics
Naval Postgraduate School
Monterey, CA. 93943-5002
6. Dr. R.J. Jost 2
System Planning Corporation
18100 Upper Bay Road
Houston, TX. 77058
7. Dr. Jim McCoy 2
NASA/JSC, Code SN3
Houston, TX. 77058
8. Dr. Nobie Stone 1
NASA/Marshall SFC, Code ES53
Huntsville, AL. 35812

9. Dr. Mario Grossi 1
Smithsonian Institution Astrophysical Observatory
Cambridge, MA. 02138
10. Professor D.E. Hastings 1
Department of Aeronautics and Astronautics
MIT
Cambridge, MA. 02139
11. Professor Lucca Minna 1
Department of Biophysical and Electronic Engineering
University of Genoa
Via all'Opera Pia 11A
16145 Genoa, Italy
12. Professor M. Dobrowolny 1
Consiglio Nazionale delle Ricerche
Istituto di Fisica Dello, Spazio Interplanetario
Via G. Galilei, Casella Postale 27
I-00044 Frascati, Italy
13. Commander, Naval Space Command 1
ATTN: N112
5280 4th Street
Dahlgren, VA. 22448-5300
14. LT. D.M. Olson 1
210 Meadowlark Lane
Duncanville, TX. 75137

